Università
Ca'Foscari
Venezia

Elettra Sincrotrone Trieste

Master's Degree
in Science and Technology of Bio and Nanomaterials

Final Thesis

The influence of graphene on the magnetism of ultrathin cobalt

Supervisor
Stefano Bonetti

Cosupervisor
Tevfik Onur Menteş

Graduand
CarloAlberto Brondin
988289

Academic Year
2019 / 2020

Abstract

Thin magnetic films with defined anisotropy are key to modern data storage technology. In this context, an important part is to investigate the effect of covering Co films with a graphene overlayer, that has shown to enhance the Perpendicular Magnetic Anisotropy (PMA) in Co [1]. Materials that shows PMA posses the net magnetization oriented perpendicular to the surface plane. The control of the PMA leads to control the data storage.

The focus of this thesis is to study the effect of the morphology and crystalline structure of graphene on the magnetic properties of Co, trying to observe a relation between PMA and the graphene quality. For this purpose, the structural properties of graphene were varied by modifying the growth methods for graphene overlayer.

In this respect, three different methods were employed based on CVD growth by ethylene as precursor for carbon atoms. The first one was by low temperature treatment of the surface, favoring the growth a graphene layer with considerable amount of disorder. In the second method by introducing oxygen acting on the formation process a more complete graphene layer was obtained though still showing some disorder. In the last one the interaction between rhenium substrate and carbon atoms was exploited to form well-oriented graphene nuclei, which were used for further growth subsequent to Co intercalation.

Synthesis and characterization were performed by LEEM/LEED for morphological and structural analysis, XPS for chemical state and XMCD, MOKE for the magnetic response of the system, using the facilities available at the Nanospectroscopy beamline at Elettra Sincrotrone Trieste.

The most important result can be summarized as the tunable quality of the graphene overlayer, which in the case of the third method consisted of a full epitaxial layer, while for the others some rotated domains are present. Consequently, more increased PMA was found in the sample with full epitaxial graphene.

Contents

List of Figures

List of Tables

Chapter 1

Introduction

The global demand for sustainable and efficient data storage results in high density, low-cost magnetic memories that have moved research interest on magnetic materials. In particular focusing on magnetic thin film systems which are perfect candidates for such applications, promising a considerable increase in data storage density and stability to thermal fluctuations. Thin films can be defined as a layer of materials having a thickness less than 1 μm, they can be made as a multilayer stack, i.e. with the superposition of thin layers of different materials. they are typically deposited on solid substrates. The choice of the right substrate is determined by the desired structural, electrical magnetic, optical properties. Thin films are suitable systems for studying the effects of reduced dimensionality on electronic and magnetic properties of the material, which can be completely different from bulk.

The material's magnetic response is governed by several factors: the dipole interaction, the exchange interaction and the magnetic anisotropy. As said before looking at the bulk the influence of these factors is different with respect to the thin film. In ferromagnetic thin films, the thickness can control the overall magnetization direction, tailoring the magnetic anisotropy and influencing the size and shape of magnetic domains. Magnetic anisotropy can derive also from the modification at the interfaces that play a role in the electronic properties, due to the lacking of the bulk symmetry. Understand and then having control of physical properties as magnetic domains can lead to important technological improvement.

Most of this thesis is based on work done at the Nanospectroscopy beamline placed at Elettra Sincrotrone Trieste, as well as on previous experiments done by the group involved. The aim of this thesis is to found a relation between magnetic properties and the graphene growth pathway in the graphene/Co/Re(0001) stack system. The main focus is the quality of the graphene layer. In addition to the linkage between morphology, crystal structure, chemical composition and magnetism.

The thesis is divided in several chapters. Chapter 2 describes the application of the techniques employed for sample characterization using two spectromicroscopy methods: Low Energy Electron Microscopy and X-ray PhotoEmission Electron Microscopy. The former allows obtaining a real space image of the surface with structural sensitivity by measuring the scattering of electrons from the electron gun. It works also in diffraction mode allowing a full crystal structure analysis of the surface. The latter instead make use of synchrotron radiation, which makes the chemical, electronic and magnetic state of the sample accessible. Both methods are surface sensitive, due to the small probing depth of low energy electrons. The last technique used in this thesis is the Magneto Optic Kerr Effect that measures the change in the polarization of the reflected visible light from a magnetic sample to measure the hysteresis loop.

In chapter 3, a short description of the two experimental setup is given: the SPELEEM and the MOKE magnetometer, both installed at the Nanospectroscopy beamline. The

SPELEEM offers lateral resolution of tens of nanometers and exploits the combined strength of LEEM and XPEEM. In particular, the use of synchrotron radiation allows imaging in real-time the magnetic structure of ultrathin films. In the other setup, the MOKE was employed to obtain information on the magnetism of the system in presence of applied magnetic fields. Both instruments are hosted in UHV chambers allowing in-situ growth and surface sensitivity.

In chapter 4, the growth and characterization of graphene/Co/Re(0001) are studied. Three different pathways for the graphene formation are illustrated, all resulting in complete graphene single layers. Moving forward in the growth method, the quality of the graphene was improved with single-orientation graphene flakes on cobalt surface were obtained.

Chapter 5, the magnetic properties of graphene/Co/Re(0001) are assessed by XMCD and MOKE. The first is a technique that exploits XPEEM for microscopy and circularly polarized light to obtain magnetic sensitivity. It allows to visualize the magnetic domains and provides a qualitative connection between graphene quality and magnetic properties. MOKE instead allows to get quantitative information on the behaviour of samples in presence of magnetic field.

In the last chapter, the main results of this thesis are resumed: "full recipe" for the complete formation of graphene/Co/Re(0001) system is summarized, pointing out the importance of surface/interface contributions in tailoring magnetic properties of this system. Among all the contributions, in this thesis is shown that the structural quality of graphene overlayer influences the magnetic anisotropy of cobalt. This result could be studied in details to understand the phenomenon and see if the same relation can be found in other combinations of ferromagnets and non magnetic materials. The next step will be the introduction of a second ferromagnet over the graphene layer and try to observe the influence of the spacer quality on the coupling between metals.

Chapter 2

Experimental methods

This section introduces the techniques used for the characterization of the multilayer system graphene/Co/Re. These include imaging of the sample surface provided by LEEM and XPEEM, crystal structure obtained by LEED, spectroscopic information from XPS, and magnetic properties assessed by XAS-XMCD and MOKE magnetometer. Thus all measurements involve the interaction with either electrons, X-rays or visible light photons with matter.

Elastic scattering of low energy electrons give rise to Low Energy Electron Microscopy (LEEM) and Low Energy Electron Diffraction (LEED). LEEM is a method able to see the surface with nanometric resolution. The contrast mechanism in LEEM is based on both chemical and structural variations of the surface. Furthermore, in ultrathin films, there is also thickness dependent contrast, as will be explained in the following. Similar to LEEM, LEED is a structural probe that can be used to fully resolve the surface crystal structure.

Interaction of X-rays with matter results in different processes, among which X-ray Photoemission Spectroscopy (XPS) and X-ray Absorption Spectroscopy (XAS) are the most important ones. XPS is done by acquiring photoelectrons originating from core level or valence band transitions. Therefore, it provides an assessment of the chemical and electronic state of samples, as well as the chemical environment. Similar to XPS, XAS gives information on the chemical and electronic state of samples. Differently from XPS, XAS measures the variations in the photon-matter interaction when photon energy is scanned to an element specific absorption threshold. In addition, magnetic information can be obtained by a polarization analysis of the XAS signal. This analysis is called X-ray Magnetic Circular Dichroism (XMCD). In this work all of these techniques are implemented in a spectromicroscopy setup, XPEEM.

Finally, interaction of polarized visible light with ferromagnetic materials gives rise to Magneto Optic Kerr Effect (MOKE). Similar to XAS it can provides magnetic information by polarization analysis, but it is not element specific. On the other hand, as this is a photon in photon out technique, it is possible to probe the sample under an external magnetic field.

The techniques listed in this chapter employ electrons except for MOKE, which uses visible light. Electrons, which travel inside a solid, are affected by the so called inelastic mean free path (IMFP), an important quantity (length) to keep in mind. This simply is the distance that electrons can travel through the medium before losing part of its energy due to inelastic scattering events. The IMFP varies with the kinetic energy of the travelling electrons roughly according to the universal curve displayed in Figure 2.1. As seen in this curve, the low energy electron range used in this work limits the probing depth to few nm. This fits well with thin film studies, where surface sensitivity is crucial.

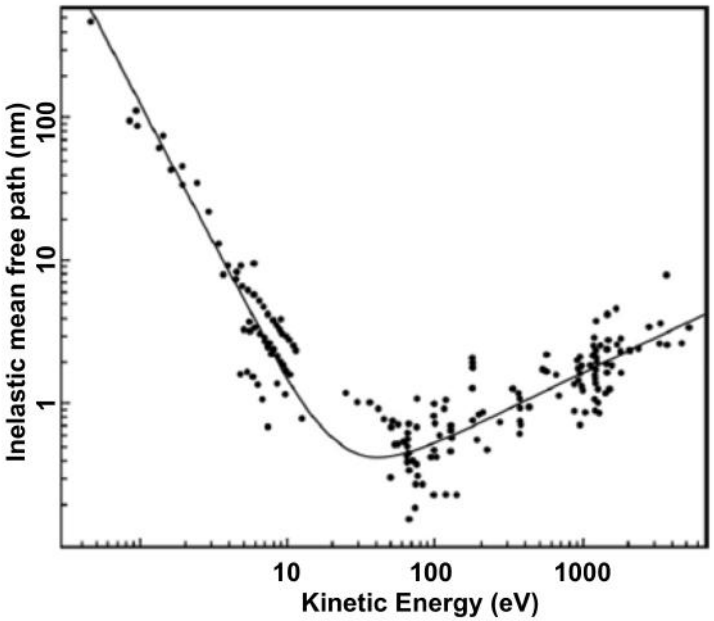

Figure 2.1: a) Electrons inelastic mean-free path universal curve in solids as a function of their kinetic energy thus allows probe few nm of the surface. Reproduced from [2]. The dots in figure are experimental data from different elements.

2.1 Low Energy Electron Microscopy

Low Energy Electron Microscopy (LEEM) is a technique based on elastic backscattering of electrons from surfaces. The electron backscattering intensity depends on the structural and chemical properties of the material.

The energy range in operating condition is 1-100 eV allowing small penetration depth which renders LEEM sensitive to surface morphology. Moreover, the high intensity of the signal in this energy range enables recording the real-time evolution of the sample surface. Surface sensitivity necessitates Ultra High Vacuum (UHV) environment in order to prevent contamination, where the pressure of the experimental chamber is kept at about 10^{-10} mbar.

LEEM imaging exploits several contrast mechanisms, depending upon the specimen. Diffraction contrast is fundamental in crystalline samples, while work function contrast is useful in amorphous materials or in presence of small crystalline grains. The contrast in general at selected energy arises from different backscattering cross section from different regions on the surface. The backscattering cross section as a function of electron energy depends on the surface crystalline structure, on the surface chemical composition, or on the work function. An example of LEEM contrast is given in Figure 2.2 a) due to elemental

differences, where the dark region is due to cobalt and the bright one to rhenium. Indeed the electron energy dependence can be used for structure determination via LEEM I-V (Intensity-Voltage).

Typically LEEM uses the specular beam i.e. the (00) reflection from crystalline surfaces. In addition to the specular beam, other diffracted beams may be used for imaging. In this case, it is necessary to select a particular diffraction spot in order to get an image which shows the domains corresponding to that diffraction spot. This imaging mode is called Dark Field modality, which helps to distinguish different coexisting structures [3].

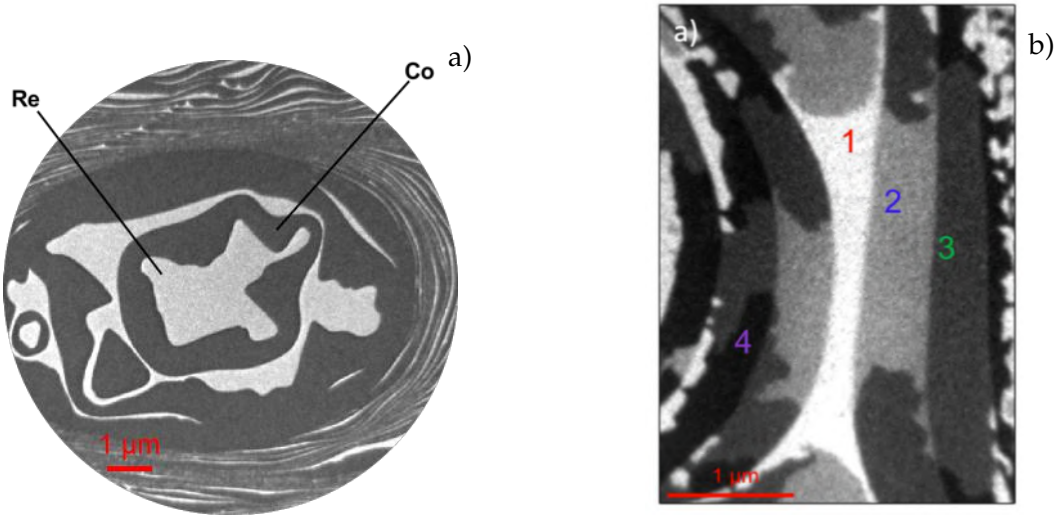

Figure 2.2: a) LEEM image at eV of Co growth on Re(0001). b) LEEM image at 19.6 eV of a multi-thickness Co/Re(0001) films. Different thicknesses are labelled where each number corresponds to ML.

Another important contrast mechanism is the interference contrast arising from height differences at atomic steps. This step contrast is based on Fresnel diffraction from two adjacent flat edges shifted by the step height and it is attributed to destructive or constructive interference between the reflected electrons from adjacent terraces.

Similar to this mechanism, there is also the quantum size contrast or quantum size effect (QSE), which is based on wave interference occurring between reflected electrons from the film surface and the substrate/film interface. This interference is sensitive to the thickness, due to the change in path difference within the crystal between electrons reflected by different layers [4]. An example of this contrast mechanism can be seen in Figure 2.2 b) where the labels in the figure represent the number of atomic layers of Co present on the surface that appear with different brightness for the particular electron energy chosen. Indeed QSE is strongly dependent on the incident electron energy. Varying the electron kinetic energy the relation between intensity and thickness can be obtained. The evaluation of the thickness of the sample can be obtained by looking at the maxima and minima of the LEEM I-V curves, where the oscillations are connected to the number of layers [5].

2.2 Low Energy Electron Diffraction

Low Energy Electron Diffraction (LEED) is a technique which shares the same electron-surface interaction with LEEM. The LEED pattern is a direct map of the two-dimensional reciprocal lattice of a crystalline surface, so it is widely used in the determination of surface crystal structure. In a LEED experiment, the electron beam is incident close to or along the

surface normal and is scattered by the localized electron density of the atoms acting as point scatterers. The crystal lattice acts as a periodical grid, therefore, constructive interferences are allowed only for specific diffraction angles and energies corresponding to the reciprocal crystal vectors.

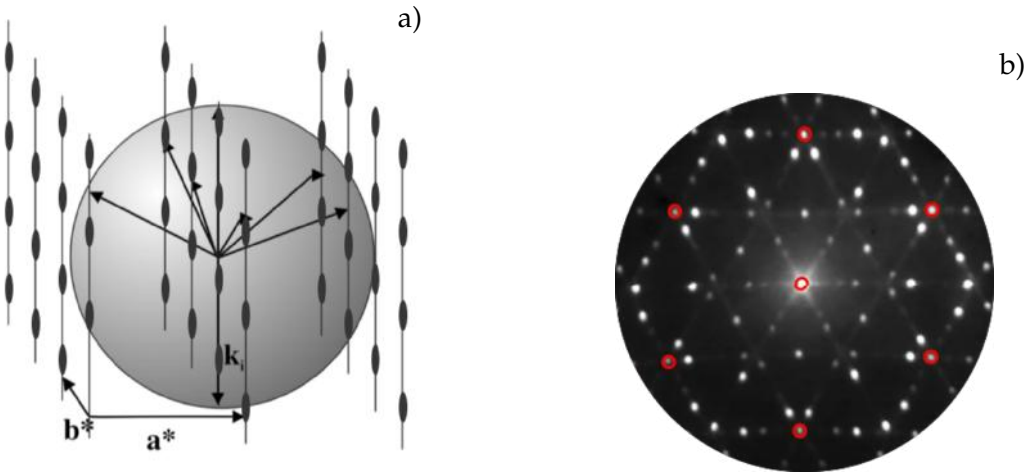

Figure 2.3: a) The Ewald's sphere representation for a thin film in LEED experiment. Reproduce d from [6]. b)LEED pattern acquired at eV of a single crystal Au(111), the spot in the middle is the (00) diffracted beam.

The diffraction spot positions in LEED pattern can be understood within the kinematic theory of scattering: according to Bragg's theory concerning the angle dependency the diffraction spots occur when the difference ($\vec{K}_{\parallel}$) between the incident scattering vector ($\vec{k}_{\parallel}$) and the scattered wavevector ($\vec{k'}_{\parallel}$) is equal to a multiple of the in-plane reciprocal crystal vector ($\vec{G}_{\parallel}$). Thus, the condition to be satisfied for film diffraction can be summarized as:

$$\vec{K}_{\parallel} = \vec{k}_{\parallel} - \vec{k'}_{\parallel} = \vec{G}_{\parallel}. \tag{2.1}$$

Similarly, the diffraction condition in $\vec{K}_{\perp}$ involves the energy dependence of the electrons. As a function of electron energy, there are also Bragg peaks along the $\vec{K}_{\perp}$. As in the case of imaging with low energy electrons, the surface sensitivity of the LEED measurement is governed by the IMFP shown in Figure 2.1. Thus, the energy-dependence of the diffraction spots become broader.

In order to describe the LEED pattern from a three-dimensional lattice, the Ewald sphere representation can be used as seen in Figure 2.3 a). The Ewald sphere radius is equal to the amplitude of the incident wavevector proportional to the squareroot of the kinetic energy of the incoming electrons. Therefore both the contributions from $\vec{K}_{\parallel}$ and $\vec{K}_{\perp}$ must be taken into account. The Eq. (2.1) is satisfied when the sphere cross the reciprocal rods [7, 8]. An example of LEED pattern can be seen in Figure 2.3 b). Energy-dependent LEED data can be used to resolve the surface crystal structure. Intensity variations depend on the electron's kinetic energy. The details of this energy dependence result from the dynamical scattering of electrons from the crystal. In dynamical scattering the single scattering approximation is no more valid. The electrons can interact even after the first scattering event, resulting in multiple scattering inside the crystal [9]. Such an experiment is called LEED I-V. A full structural determination can be accomplished from LEED I-V data using theoretical modelling that takes into account the dynamical scattering.

2.3 Magneto Optic Kerr Effect

The interaction of light with matter provides information also on the magnetic properties of the materials. Magneto optical (MO) effects in magnetic materials arise due to the optical anisotropy originating from the magnetization $\vec{M}$ which can be influenced by external forces such as magnetic fields. The MO effect corresponds to a change in the state of light polarisation upon interaction with magnetic materials. Such effects are typically observed in reflection (termed as Kerr effect) and in transmission (Faraday effect) as a rotation of the polarisation of the light. In order to understand the Kerr effect, the eigenstates of the dielectric response of a magnetic medium have to be considered, which correspond to circular polarisation states.

Linearly polarized light can be thought as a superposition of left circularly polarized and right circularly polarized light. The two circular polarisation states interact with the magnetic medium with different strengths. This results in a different amplitude and phase shift for the reflected left and right circular polarized light. Thus the initially linearly polarized incident light will be slightly elliptically polarized and rotated by a few degrees after reflecting off the sample [10, 11]. The optical properties of materials are described in terms of its generic dielectric tensor ε.

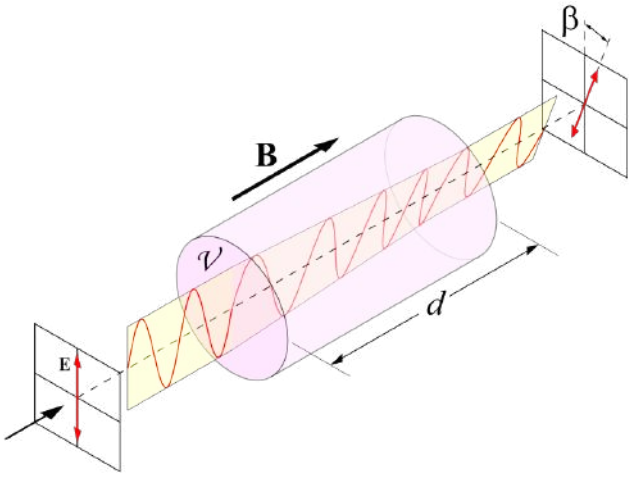

Figure 2.4: Linear polarized light passing through a magnetic media in presence of magnetic field. The transmitted light results rotated by an angle proportional to the magnetization of the medium. The same effect is found in reflection, i.e. Kerr effect. Reproduced from Wikipedia.

This dielectric tensor can be divided in symmetric and antisymmetric components. The symmetric part, in case of isotropic media without any external field, reduces to only the diagonal components, and hence the so called dielectric constant. In the presence of spontaneous magnetization or a magnetic field, for example along Z-direction, the dielectric tensor ε reduces to 2.2 where the the off diagonal components $\varepsilon_{yx}(\mathbf{M})$ are different from zero and they become function of the magnetization vector of the material [12]. Thus the linear polarized light after reflection possesses light component in both x and y direction, resulting rotated. A simple sketch in Figure 2.4 helps to visualize the Kerr effect.

The non-vanishing off diagonal terms in a magnetic sample are proportional to the directional cosine of the magnetization vector. This affects the velocity of light and as a consequence left-circularly polarized and right-circularly polarized light experience different refractive indices. Thus traveling with different velocities inside the material. When they have reflected away they will result in phase shift. The recombination will be evidenced in a rotation of the polarization plane of the light [13].

$$\varepsilon = \begin{pmatrix} \varepsilon_{xx} & \varepsilon_{xy} & 0 \\ \varepsilon_{yx} & \varepsilon_{yy} & 0 \\ 0 & 0 & \varepsilon_{zz} \end{pmatrix} \tag{2.2}$$

$$\begin{aligned} \theta_K(\mathbf{M}) &= \frac{\pi}{\lambda}(n_+(\mathbf{M}) - n_-(\mathbf{M}))d \\ n_\pm^2(\mathbf{M}) &= \varepsilon_x \pm i\varepsilon_{xy}(\mathbf{M}) \end{aligned} \tag{2.3}$$

The resulting Kerr rotation θ_K Eq. 2.3 is linked to the dielectric tensor 2.2 by means of the refractive index n in Eq. 2.3.

Kerr effect can be observed in different experimental geometries as can be seen in the sketch in Figure 2.5 a),b). These geometries are described by the orientation of the magnetization with respect to the sample plane and incident light:

- Longitudinal Kerr effect, the sample magnetization lies in the surface plane ("in-plane") as well as in the scattering plane made of the incident and reflected beams.
- Polar Kerr effect, the magnetization is perpendicular to the sample plane ("out-of-plane").

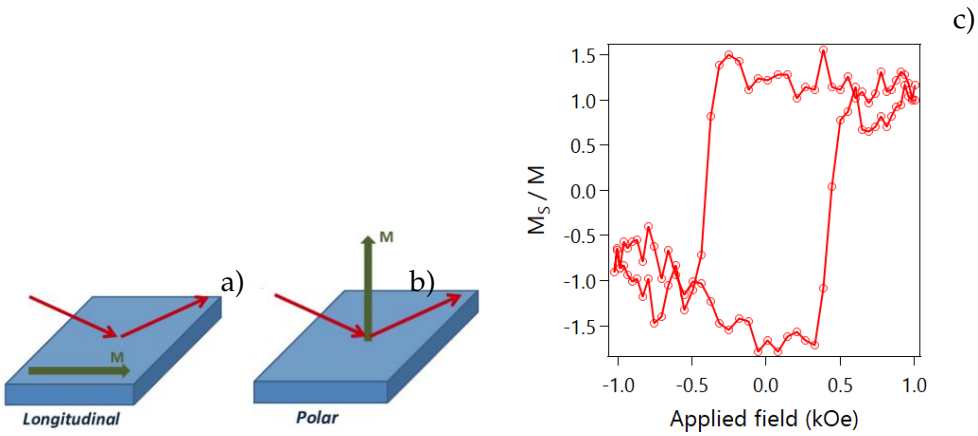

Figure 2.5: Representation of the different configurations for MOKE measurements. M means magnetization and the red line stands for the direction of the laser light. Two configurations are shown: a) longitudinal, b) polar. c) Example of hysteresis loop obtained in polar MOKE experiment.

MOKE signal is suitable to study surface magnetism due to the limited penetration depth of visible light in metals, usually tens of nm, as well as the lock-in method typically used to extract the small magnetic signal [14, 15]. As a result, hysteresis loops can be measured from ultrathin ferromagnetic films giving a relation between the applied magnetic field and the strength of the magnetization component along the measurement direction [16].

An example of the magnetic hysteresis measured by polar MOKE can be seen in Figure 2.5 c). Applying a magnetic field to a ferromagnetic material the magnetization increases with increasing field. At the saturation point where all the magnetic domains are aligned, as can be noticed in the flat region of the loop at high field. When the applied magnetic field is reduced back to zero, a nonzero value of magnetization remains, called the remanence magnetization. Upon reversing the field, the point at which the magnetization is zero is called the coercive field, and the force applied to remove residual magnetization is called the coercive force.

2.4 X-ray spectroscopies

2.4.1 X-ray Photoemission Spectroscopy

The X-ray photoemission spectroscopy (XPS) is based on the so called photoelectric effect. This effect arises when a photon impinging to a material possesses enough energy to remove an electron from its bound state and excite it to the vacuum level. The kinetic energy E_k and the number of the emitted photoelectrons are typically measured using an energy-dispersive analyzer. The binding energy of the electron can be obtained from the photon energy $h\nu$, the kinetic energy E_k of the photoelectrons and the work function ϕ of the surface, via the relation:

$$E_b = h\nu - E_k - \phi \tag{2.4}$$

The binding energies of core-level transitions vary from few tens of eV to several keV which matches well with the energy range of x-ray radiation. The photon energy must be chosen properly in order to optimize the photoionization cross section for the particular core-level of interest, which can be done thanks to the tunable photon energy at a synchrotron source.

The binding energy of the core-level is specific for the corresponding element making XPS a chemically-sensitive probe.The atoms probed feel different chemical environment. As a result, their binding energy is not unique and it is distributed in an energy range. The difference in binding energy between different atomic sites in a material is termed as core-level shift (CLS). This can arise from defect or vacancy, different atomic neighbours or structural differences.

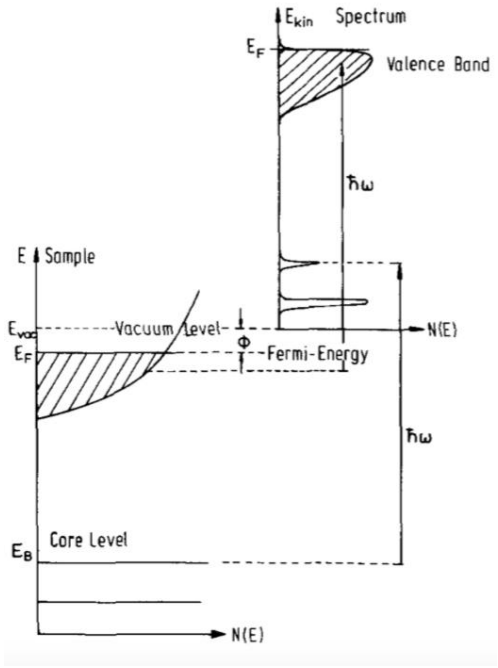

Figure 2.6: Sketch of simplified electronic structure and relative photoemission spectra. The E_k in abscissa is usually substituted by E_b. In solids E_b is referred to E_F while in free atoms is referred to the vacuum level E_{vac}. Reproduced from [17]

Photoemission process can be described in three stages:

- a photon is absorbed and an electron is excited, this is called photoionization;
- the excited electron moves through the sample to the surface;

- the electron escapes from the surface.

Inelastic mean free path and work function considerations come from the second and third steps, respectively. In the energy range of the XPS experiments the IMFP, shown in Figure 2.1, is a fundamental parameter determining the escape depth of electrons from the material, which is typically only a few nm. The relatively short electron mean free path makes XPS a surface sensitive technique. Thus, Ultra High Vacuum (UHV) plays a crucial role in XPS experiments in order to preserve the surface cleanliness [17, 18].

The sketch in Figure 2.6 helps to visualize the process producing the photoemission spectra. The binding energy E_b of an energy level measured by XPS in solids is referred to the Fermi level[17]. The exact energy of the core-level photoelectrons depends sensitively on the screening process occurring after the formation of the photohole.

After photoionization, the screening of the positive charge associated with the hole results in slightly different energy of the photoelectron. On the other hand, the excitations created during the photoemission process, such as plasmons, determine the lineshape of the core-level spectrum. These excitations can be divided into intrinsic and extrinsic plasmons:

- intrinsic plasmons arise from the photoemission process;
- extrinsic plasmons are due to the photoemitted electrons that produce excitation in other parts of the solid.

These excitations with the contribution of energy losing processes as electron-electron and electron-ion collisions lead to an asymmetric XPS lineshape [17].

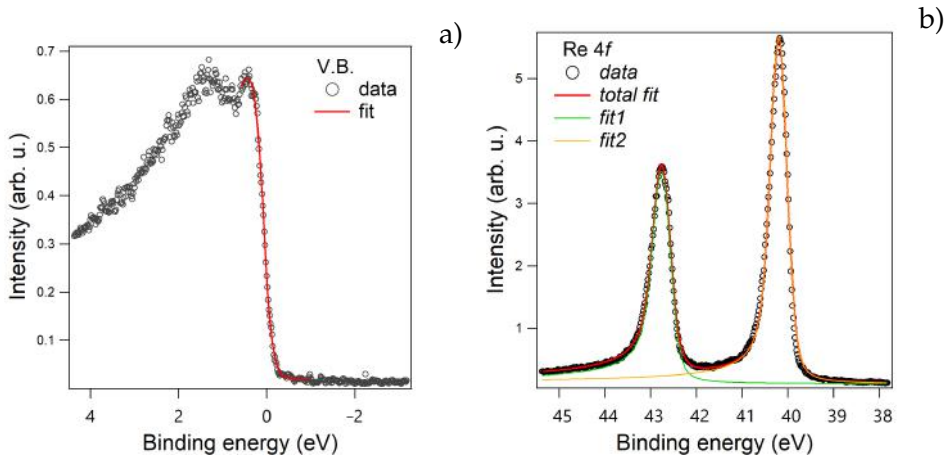

Figure 2.7: a) The XPS spectra acquired at the valence band of the material it gives the value of the Fermi energy E_F for the detemination of the E_b. b)XPS spectra and its fitting curves using Doniach-Sunjic methos.

the asymmetric core-level lineshape is fitted using a form by Doniach-Sunjic (DS)[19]. An example can be seen in Figure 2.7. Figure 2.7 a) shows the evaluation of the the Fermi level Figure 2.7 b) instead shows the DS fit to the Re 4f core-level doublet. The method provides the simulation of the photoemission spectral lines based on the convolution of a Gaussian and Lorentzian curve along with an asymmetry coefficient.

The asymmetry coefficient accounts for the asymmetric lineshape mentioned above. The Gaussian width collects the instrumental broadening contributions from the photon source as well as the energy analyzer, the Lorentzian width describes the lifetime of the core-hole generated by the photoioniziation. Surface defects and grain boundaries also may affect the peak shape resulting in broader peaks as will be seen in the results section.

2.4.2 X-ray Absorption Spectroscopy and X-ray Magnetic Circular Dichroism

X-ray Absorption Spectroscopy (XAS) is a spectroscopic technique based on the photon-energy dependent interaction between x-rays and matter. In XAS, an electron from the core level is excited by a photon and if it has enough energy can leave the materials. This condition is allowed by the use of synchrotron radiation for which the photon energy is continuously tunable.

The resonant condition is found at an absorption edge. The absorption process is element-specific and from the analysis of the spectrum, it is possible to obtain the chemical state of the atoms.

XAS is usually performed at the core level absorption edge indicated by a letter and a number depending on the particular core level. The letter depends on the principal quantum number (K, L, M etc, for n = 1, 2, 3...) whereas the number derives from the subshell (1, 2, 3 etc from s, $p_{1/2}$, $p_{3/2}$...).

In most studies, the soft x-ray regime below 1 keV is particularly important in near-edge spectroscopy, due to transitions which include the K edges of carbon, oxygen, and lighter elements and L, M, and N edges of transition metals. The former ones allow to access the study of organic-based materials such as graphene. The latter are crucial in chemical and magnetic studies of metals and metal-oxides.

The absorption edge may also be exploited for the assessment of the magnetic state of the sample surface. At certain resonances, the magnetic contribution to the XAS signal becomes substantial [20, 21]. The technique used to extract this magnetic contribution is called X-ray Magnetic Circular Dichroism (XMCD), which is based on a polarization analysis of the XAS signal near the X-ray absorption edge. The result depends on the size and direction of the net magnetic moment. XMCD has been extensively used at the dipole transitions, e.g. 2p to 3d ($L_{2,3}$ edge) transitions for 3d transition metals exploiting the strong spin-orbit splitting of the 2p core level [10].

The XMCD effect can be described as left and right circularly polarized light absorbed differently. The overall XMCD signal is defined as the difference between two absorption spectra acquired with opposite polarization and divided by their sum:

$$I_{XMCD} = \frac{I^L - I^R}{I^L + I^R} \tag{2.5}$$

where I^L and I^R are the absorption signals with $left$ (L) and $right$ (R) photon polarization, a complete derivation can be found in the literature [10, 22]. Note that the XMCD signal is proportional to the component of the net magnetization vector along the beam direction, thus geometry considerations have to be made for the measurements.

2.4.3 X-ray PhotoEmission Electron Microscopy

X-ray PhotoEmission Microscopy (XPEEM) uses soft X-ray photons to generate photoelectrons which are used to probe the state of the irradiated sample. XPEEM shares the same lens apparatus with LEEM which accelerates the photoelectrons to the imaging column of the instrument. Tunable high-brightness X-ray beams from the synchrotron extends the application field of XPEEM instruments, which can achieve chemical, magnetic and electronic structure contrast by several kinds of spectroscopies.

XAS-PEEM collects the secondary electrons from the sample. In this way, it is possible to obtain laterally resolved XAS spectra as a function of photon energy. Moreover, XAS-PEEM used with circularly polarized light, provides dichroic signal from the sample, which can be used to obtain the distribution of magnetic domains on the sample surface. Instead of secondary electrons, using core level or valence band photoelectrons the instrument can be used to perform XPS-PEEM, which reveals different chemical species.

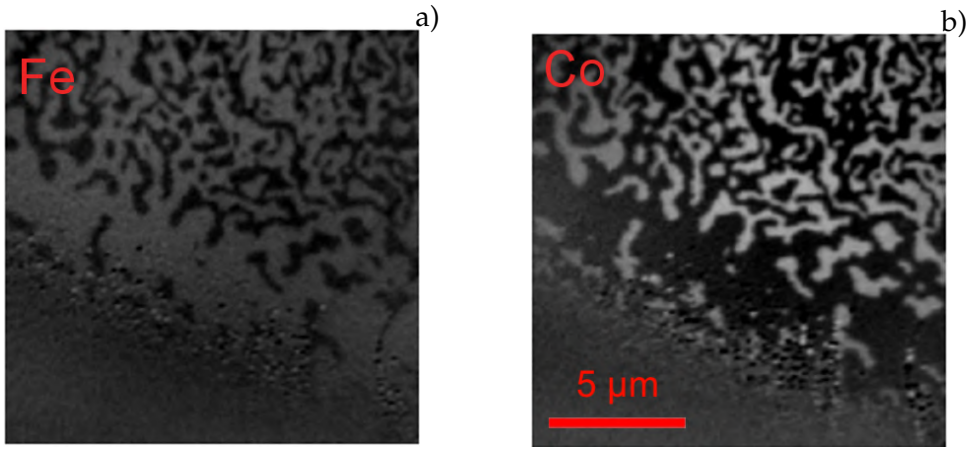

Figure 2.8: XMCD images acquired at room temperature of a multistack Fe/graphene/Co/Re(0001), showing magnetic contrast. a) XMCD-PEEM image acquired at Fe L_3 edge 708 eV. b) XMCD-PEEM image acquired at Co L_3 edge 780 eV. The images acquired in the same region of the sample show a strong AFM coupling between Fe and Co.

XMCD-PEEM is based on the same analysis as in Eq.(2.5). Thus the XMCD image is obtained as the difference of two images obtained with opposite circular polarisation. As an example, Figure 2.8 shows XMCD images of the same region of a Fe-Graphene-Co sample acquired at photon energies corresponding to Fe and Co L_3 edges. The chemical selectivity of such a measurement is evident: selecting the proper photon energy allows the visualization of the magnetic state of a single element. As can be appreciated in Figure 2.8 a) and b), the element-specific XMCD measurement reveals that the sample shows AFM coupling, where the contrast in the Co L_3 image is opposite to that of the image taken at Fe L_3. AFM stands for antiferromagnetic, AFM coupling occurs in ferromagnets that can interact, such that the magnetization vectors inside each ferromagnet have an opposite direction to the other [23, 24].

Chapter 3

Experimental setup

This thesis work was carried out using two instruments both using the interaction of electromagnetic radiation with matter: SPELEEM (using X-rays) and MOKE (using visible light). The former takes advantage of synchrotron radiation as a high-intensity photon source with tunable energy and polarization in order to study the electronic structure, chemical and magnetic state of materials. The latter, instead, uses visible light with variable polarization to study magnetism. All the experiments were performed at Nanospectroscopy beamline at Elettra Sincrotrone Trieste.

The Spectroscopic PhotoEmission and Low Energy Electron Microscope (SPELEEM) is a combined LEEM-XPEEM instrument that allows probing both with photons (XPEEM) and electrons (LEEM). It can provide morphological structural and chemical information in a laterally-resolved manner. In addition, in microspot diffraction mode it can probe crystal structure (μ-LEED) and electronic structure (μ-ARPES).

MOKE magnetometer essentially is composed of a laser light source, two polarimeters, an electromagnet, PEM, lock-in amplifier and a detector, in order to collect a magnetic signal.

3.1 Spectroscopic Photoemission and Low-Energy Electron microscope

The Spectroscopic PhotoEmission and Low Energy Electron Microscope (SPELEEM) is the combination of a LEEM with XPEEM that allows a multimethod characterization of samples. The SPELEEM at the Nanospectroscopy beamline of Elettra uses synchrotron radiation as probe and it is capable of achieving XPEEM, μXPS, XAS-PEEM, XMCD-PEEM, ARPES, for chemical and magnetic assessment, whereas morphology and crystalline structure is provided by LEEM/LEED [25].

In the Figure3.1a) a picture of the SPELEEM sketches the pathway of the electrons (blue, LEEM) and photons (red, XPEEM) . Photons come from the synchrotron source while electrons are produced bt an electron gun (LaB_6). The latter are accelerated and decelerated at the specimen by a bias voltage between sample and electron optics. Electrons or photons interacting with the sample result in elastically backscattered or photoemitted electrons, respectively, which all are directed by electromagnetic lenses into the energy analyser and finally to the detector. The detector is composed by Multi-Channel-Plate electron multiplier, a phosphorus screen and a CCD camera.

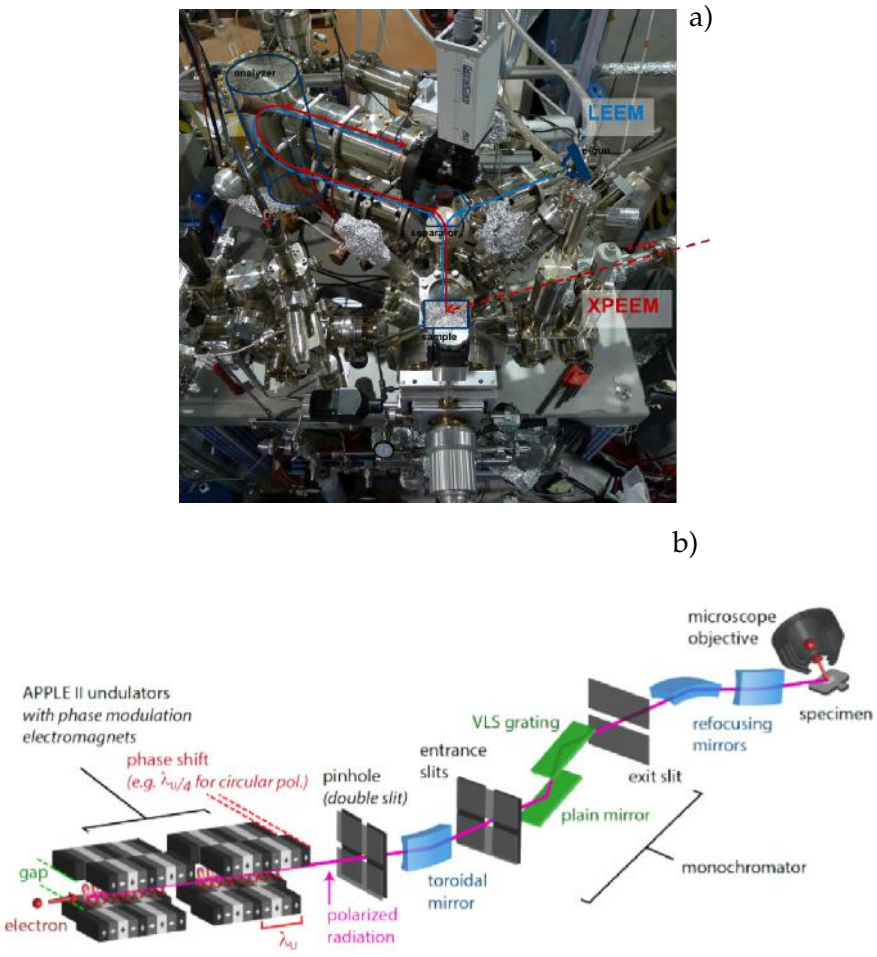

Figure 3.1: a) Picture of the SPELEEM at Nanospectroscopy in Elettra Sincrotrone Trieste, a scheme was superimposed, in order to help to visualize the electrons and photons pathway. Reproduced courtesy of Menteș T.O. b) Nanospectroscopy beamline scheme. The two undulators can be set to generate photons with a specific energy and polarization. A pinhole stops unwanted radiation, the selected radiation passes through a toroidal mirror before entering in the monochromator. The width of the exit slit determines the final energy resolution. The refocusing mirrors finally produce a small beamspot on the specimen.

The photons are generated by two APPLE II type helical undulators, which have a relative phase adjusted by a magnetic deflector. These elliptical undulators allow to obtain polarized light horizontal and vertical (linear), and left and right (circular). The energy of the photon beam can be selected by a Variable Line Spacing (VLS) monochromator. Refocusing mirrors focus the monochromatized beam on the specimen. A simple sketch of the beamline can be seen in Figure3.1b), and a detailed resume of the performance of the beamline can be found in Appendix A.

In LEEM and XPEEM modes, the microscope can reach a lateral resolution of better than 10 nm and 30 nm [26], respectively. In addition to real-space imaging, the SPELEEM can also work in diffraction mode or reciprocal-space imaging. A micrometric size aperture (called *field limiting aperture*) can be placed in the image plane of the illumination column, allowing micro-probe LEED (μ-LEED) or ARPES (μ-ARPES).

In order to obtain the diffraction pattern, the backfocal plane of the objective lens is transferred to the detector. The energy filter is useful especially in the μ-ARPES mode to filter the photoelectron energies, but it is also used in μ-LEED for eliminating inelastically scattered and secondary electrons from the background.

The SPELEEM reaches its highest energy-resolution in μ-XPS mode, in which the local spectra are obtained by acquiring spectral images at the dispersive plane of the energy analzyer. Different parts of the spectrum is accessed by varying the photoelectron energies via the sample bias voltage V_{st}. Similarly to the microspot diffraction mode, μ-XPS is performed by selecting a micron-sized area using the *field-limiting aperture* at the image-plane of the objective lens, and by transferring the dispersive plane of the energy analyzer to the detector using projector lenses. The dispersive plane appears as a line, along which the intensity profile represents the photoemission spectrum. In this operating mode the SPELEEM can reach an energy resolution better than 200 meV[26].

3.2 Magneto Optic Kerr Effect

The experimental setup for the Magneto Optic Kerr Effect (MOKE) measurements is composed of a UHV chamber and an optical table. Importantly, the MOKE setup is designed to be compatible with the SPELEEM sample holder. Moreover, it has a transfer chamber in order to exchange samples with the SPELEEM instrument without having to break vacuum.

The MOKE chamber, as seen in Figure3.2a), is set up in two levels, in which the upper part is dedicated to sample preparation, and the lower part is where the MOKE measurements are carried out. This configuration enables in-situ growth and characterization of samples within the same vacuum housing. In the upper parts are placed e-beam evaporators and a sputter gun for sample cleaning. The sample manipulator along with translation and rotation provides also the possibility to heat and cool the sample. The chamber is kept at 10^{-10} mbar by a pumping system, composed of two turbomolecular pumps, one ionic pump and an ion getter.

In the lower level, a UHV-compatible electromagnet is placed, which allows to reach a magnetic field of $\pm$ 150 mT. The optical bench is tightly fixed on chassis sustaining the chamber making it mechanically more robust. The light sources is a stabilized red HeNe Laser, with an output power of 1.2 mW and wavelength of 632.991 nm, which allows to operate in both intensity and wavelength stabilized modes.

Two measurement configurations are available. In the polar configuration, the laser beam impinges on the sample at normal incidence, passing through a small circular opening in one of the magnet's poles. Two mirrors (M1,M2) facilitate laser alignment and a lens (FL1) permits a precise focusing. After reflection from sample and beam splitter (BS), the beam passes through the photoelastic modulator and finally after being refocused im-

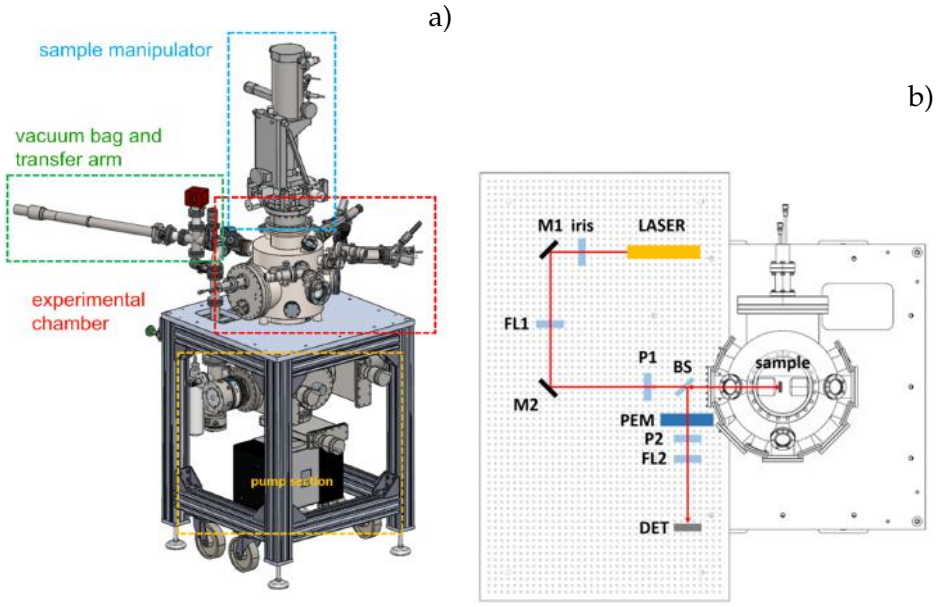

Figure 3.2: a) 3-D digital reproduction of the UHV MOKE apparatus, highlighted in the figure the principal components. b) Scheme of the optical bench in the configuration for polar MOKE.

pinges on the detector. The photoelastic modulator (PEM) modulates the polarization of the laser beam at high frequency (f=50kHz), permitting signal filtering and amplification by means of a lock-in amplifier [27].

In order to carry out the MOKE measurement, two polarizers (P1,P2) are inserted in the optical path: the first defining the polarization of the incoming laser beam, and the second used to optimize the sensitivity to the magnetic signal after interaction with sample. A technical drawing of the optical bench in the polar configuration is shown in Figure3.2 b).

In the longitudinal MOKE configuration of this setup the laser beam impinges on the sample at about 45° incidence angle, while the sample is oriented between the electromagnet poles in such a way that the magnetic field is parallel to the sample surface. Furthermore, the field is also aligned with the scattering plane, as explained in the previous chapter. Differently from polar MOKE, no beam splitter is needed in this configuration, as the incoming and reflected beams do not need to be separated.

The MOKE signal is extracted by using a photoelastic modulator (PEM) together with lock-in methods[27]. The signal from such a setup can be analyzed using Mueller matrices and Fourier series. Small angle approximation can be used because typically both the Kerr rotation angle φ_K and the Kerr ellipticity ϕ_K are small numbers. The intensity of light as a function of time that arrives at the detector may be calculated, after Fourier expansion and simplification leads to:

$$I(t) = I_0[1 + 2\varphi_k J_0(A_0) - 4\phi_k J_1(A_0) sin(2\omega t) + 4\varphi_k J_2(A_0) cos(2\omega t)] \tag{3.1}$$

where I_0 is the DC intensity or the "average" intensity, $\omega = 2\pi f$ is the angular frequency of the PEM oscillations and A_0, the retardation amplitude of the PEM. Three voltages are also measured: V_DC, V_1f and V_2f that are DC signal and the 2 PEM harmonics respectively, $J_1(A_0)$ and $J_2(A_0)$ are the Bessel's function proportional to the ratio between PEM harmonics and DC signal[28]. Thus the Kerr angle φ_K and the Kerr ellipticity ϕ_K are:

$$\varphi_K = \frac{\sqrt{2}}{4J_2}\frac{V_{2f}}{V_{DC}} \qquad \phi_K = \frac{\sqrt{2}}{4J_1}\frac{V_{1f}}{V_{DC}}. \tag{3.2}$$

The experiment is robust against small fluctuations by taking the ratio of the AC term to the DC term. The full derivation can be found [29].

Chapter 4

Growth pathways for graphene/Co/Re(0001)

The objective of this thesis is to grow and characterize graphene/Co/Re(0001) as a stack with strong and controllable perpendicular magnetic anisotropy PMA, with well-defined out-of-plane magnetization. In order to achieve this result, several graphene formation pathways are presented as a key point for the optimization of the graphene/Co/Re preparation.

Focusing on a systematical spectro-microscopical characterization of the resulting graphene layer, the target is to outline the role of the growth method on the structural quality of the graphene layer, its chemical state and its interaction with the metal surface. The characterization of the stack system was performed at the beamline Nanospectroscopy at Elettra Sincrotrone Trieste, where the SPELEEM and MOKE magnetometer can provide complete structural, chemical, magnetic evaluation of the system.

Starting from a Co/Re(0001) ultrathin film grown by the well-known procedure established in earlier works by the group, graphene was grown by thermal induced graphitization of a carbon precursor, which was ethylene (C_2H_4) for all the experiments. Three different graphene growth pathways were considered. In the first one, a precise gas dose and annealing to moderate temperatures (about 400 °C led to the formation of a complete graphene layer that presents domains with differential azimuthal orientation along with considerable structural disorder.

In the second method, the graphene quality was enhanced by introducing oxygen in the chamber during graphene formation. oxygen was added in order to lower the nucleation density during graphene growth. Indeed, this resulted in graphene sheets of similar azimuthal distribution of domains, but with a considerably improved order reflected in sharper diffraction spots.

Finally, in the third method, the interaction between Re(0001) and graphene was exploited in order to induce the correct graphene orientation. This was accomplished by growing initially small graphene flakes directly on the Re(0001) surface forming an incomplete graphene layer. Then cobalt was deposited, which intercalates between Re(0001) and graphene. Thus, there are epitaxial graphene seeds on cobalt at this stage. Dosing ethylene at high temperature completes the graphene layer resulting in a single graphene sheet on cobalt composed of nanometric flakes all with the same epitaxial orientation.

4.1 Overview of thin film growth

Thin films can be defined as materials that posses one dimension much lower than the other two. They usually present thicknesses between nanometers (10^{-9} m) and micrometers (10^{-6} m). They can be composed of a single layer or a multilayer. They are created by condensation of atomic species on a substrate, using a variety of methods among which there is also thermal evaporation, used in this work.

In this thesis two methods are employed: electron beam physical vapour deposition (EBPVD) and chemical vapour deposition (CVD), for cobalt deposition and, respectively for graphene formation. Physical vapour deposition consists of the condensation of vaporized material on the substrate surface, under vacuum conditions. The material to be deposited is transformed from solid to vapor by heating. Some atoms in the vapor phase reach the substrate and stick to the surface. This deposited material goes through coalescence on the surface, i.e. it condenses and forms a film. The sublimation sources used in this thesis are e-beam evaporators, in which the evaporant is heated by electrons ejected from a filament.

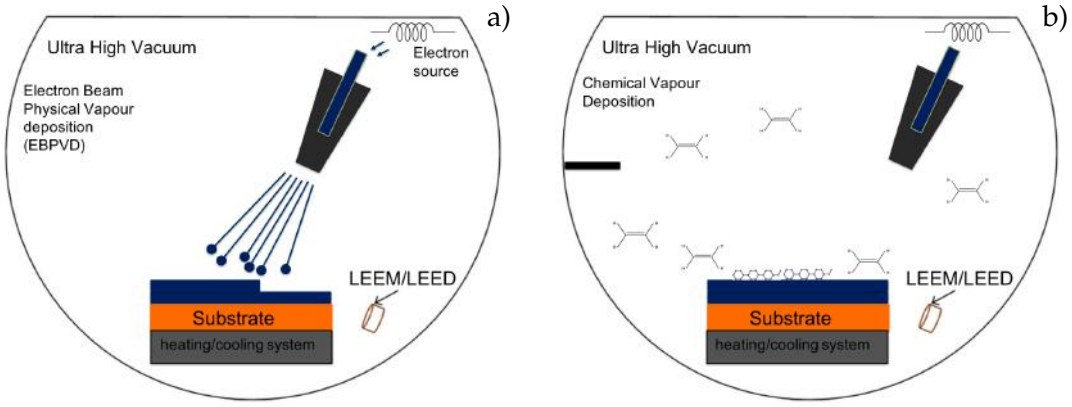

Figure 4.1: a) Simple schematics of the experimental chamber and evaporator for metals deposition. b) Simple schematics of the experimental chamber during the chemical vapour deposition for graphene formation. The chamber is under ultra high vacuum conditions with base pressure 10^{-10} mbar. The substrate is placed on a cartridge able to heat the sample up to 2000°C, in the chamber, LEEM/LEED provides real time observation of the sample surface.

A simple representation of the growth environment and deposition process can be seen in Figure4.1 a) where the blue lines depict the atoms ejected from the metal. These have a ballistic trajectory to the substrate surface, so the evaporator must point at the substrate for obtaining a correct deposition.

This method provides deposition of a single layer of atoms, which can be termed as an atomic layer or monolayer (ML).Note that, one should specify whether the ML units correspond to the layer density of the substrate or the adsorbate. The chosen substrate is Re(0001) with lattice parameter a = 2.761 Å, while for *hcp* cobalt a = 2.507 Å, and the mismatch between unit cells is less than 10%. Therefore, 1 ML of cobalt is $\sim$ 20% denser concerning Re superficial atomic density. In this thesis, ML units will refer to the atomic density of a bulk-like Co layer.

The interatomic distance between successive layers is due to the cell parameter for *hcp* c = 4.07 Å. After the deposition of the first layer (the more strained), the others are packed by roughly 0.2 nm/ML, which can be considered as another thickness unit for cobalt deposition[30].

Chemical vapour deposition refers to the deposition of adsorbates via a chemical reaction near or at the surface of the sample. CVD is a thermodynamic complex process

that involves molecular adsorption, desorption and dissociation under specific conditions such as temperature, pressure, reaction rates and energy transport. For this purpose, by selecting the right parameters it is possible to tune the quality of the deposited layer. The entire CVD process can be divided into a few steps:

- The introduction of the reactants or precursor in the chamber.
- The adsorption of moleculesin gas phase on the substrate surface.
- Diffusion of precursors over the surface.
- Reaction on the surface thus the formation of the layer.
- Desorption of unreacted species.

4.2 Rotationally incoherent Graphene

4.2.1 Cobalt deposition on Re(0001)

The first task for the realisation of graphene/Co/Re stack is the deposition of few ML of cobalt over rhenium(0001) surface. This was achieved by EBPVD: Co was sublimated from a high purity rod by electron beam bombardment and the Co atoms were deposited on Re. The Re substrate possesses the same hexagonal structure as the Co film, so *epitaxial* growth is favoured.

The first ML deposited is affected by considerable strain due to the lattice mismatch between the two metals. In this case, Co and Re unit cells differ by about $\sim 10\%$. In order to obtain a well-ordered complete monolayer, the first Co layer was deposited at 360 °C. The pressure within the chamber was about 10^{-10} mbar during the deposition process, which helps to avoid contamination of the substrate. The deposition rate was selected to be about 5 min/ML based on previous experiments layer-by-layer growth.

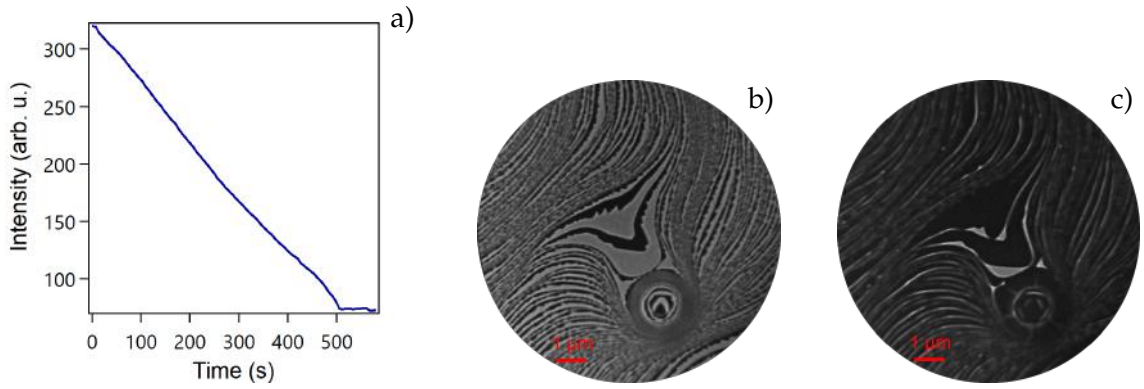

Figure 4.2: a) LEEM I-t acquired at 8 eV, average LEEM intensity as function of time for the deposition of the first layer. LEEM images of cobalt on Re (0001) growth movie at 360 °C, Field of View is 10µm, the electron energy is 8 eV. b) Image taken in the first stage of the growth, around 100 seconds. c) Image taken after 450 seconds from the beginning of the cobalt deposition, when almost the film is complete.

The formation of the first ML was followed by LEEM. The intensity of the signal is collected as a function of the time (LEEM I-t, intensity vs. time) as shown in Figure 4.2 a). The electron energy in the LEEM measurement is chosen so that the reflectivities of the Re and Co are different. At this electron energy, the intensity decreases as the Co coverage increases. Two frames from the real time observation are displayed in the Figure 4.2 b) and c).

The image in Figure 4.2 b) shows the Re surface after ~ 100 seconds from the beginning of the deposition. In this image the dark regions correspond to Co and the bright regions are Re. The Co propagates from the terrace boundaries without the formation of other nucleation points on the Re terraces. The Co ML grows until it covers the entire Re surface, as seen in Figure 4.2c). The Co ML was complete at around 500 seconds. This value also provided a calibration for further growth, i.e. we assumed a deposition rate of 500 s/ML.

The deposition of additional 3.7 ML of cobalt was done at room temperature and followed by LEEM as the first ML. This allows to grow a uniform film and to avoid film rupture.

Figure 4.3 a) shows the time evolution of the LEEM intensity. The first minimum is the completion of the second ML, the following maximum is the closure of the third ML and subsequently, the third minimum, is the fourth ML. After the last minimum the evaporation is continued until the completion of 4.7 ML coverage. The time interval between

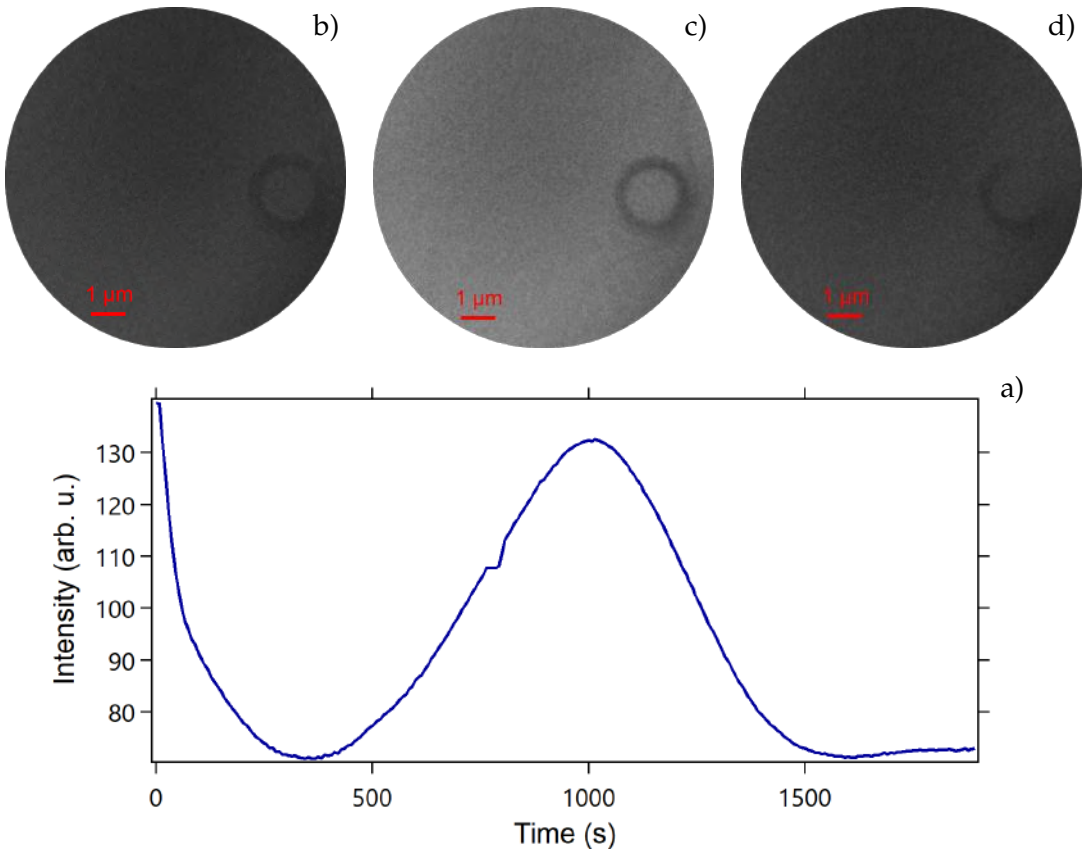

Figure 4.3: a)LEEM I-T corresponding the formation of slightly more than 3 layers of cobalt on the 1 ML cobalt already deposited on Re(0001). LEEM images of cobalt multilayer growth movie at RT, Field of View is 10 μm, the electron energy is 8 eV. The three images correspond to three different layers formed: b) 2 ML, c) 2 ML, d) 4 ML.

the formation of each layer is in agreement approximately with the deposition time reported for the first ML. This provides a crosscheck on the calibration obtained during the monolayer deposition.

Figure 4.3 reports also 3 LEEM images that are frames taken from the real time observation. Figure 4.3 b) represents the surface after the deposition of 2 MLs, while in c) 3 MLs and d) the 4 MLs are shown. As seen in the LEEM images, the surface appears uniform within the LEEM resolution. The absence of contrast in the images is proof of layer-by-layer growth.

In order to obtain information about the number of layers deposited, the LEEM I-V spectra were compared with spectra from reference samples that possess similar thickness of cobalt. The LEEM intensity as a function of electron energy shows thickness dependent oscillations due to the Quantum Size Effect (QSE) as mentioned chapters 2. In Figure 4.4 a), four LEEM I-V spectra are shown. The Red curve is the spectra from the current experiment, while the two grey curves are reference spectra obtained from films of 4 and 5 ML Co on Re(0001). The correlation between atomic layers and the number of peaks in the spectra is easily seen in the grey reference curves. For a better evaluation a reference spectrum with a 70/30 of weighted contributions from 4 ML and 5 ML spectra was created as seen in dotted line in Figure4.4 a). The result is plotted together with the experimental curve from the 4.7 ML Co film.

In order to better compare the simulated and measured spectra from the 4.7 ML Co film , the derivative of the LEEM intensities are compared in Figure 4.4 b). As can be seen from the figure, the derivatives allow to highlights small variations. The experimental spectrum

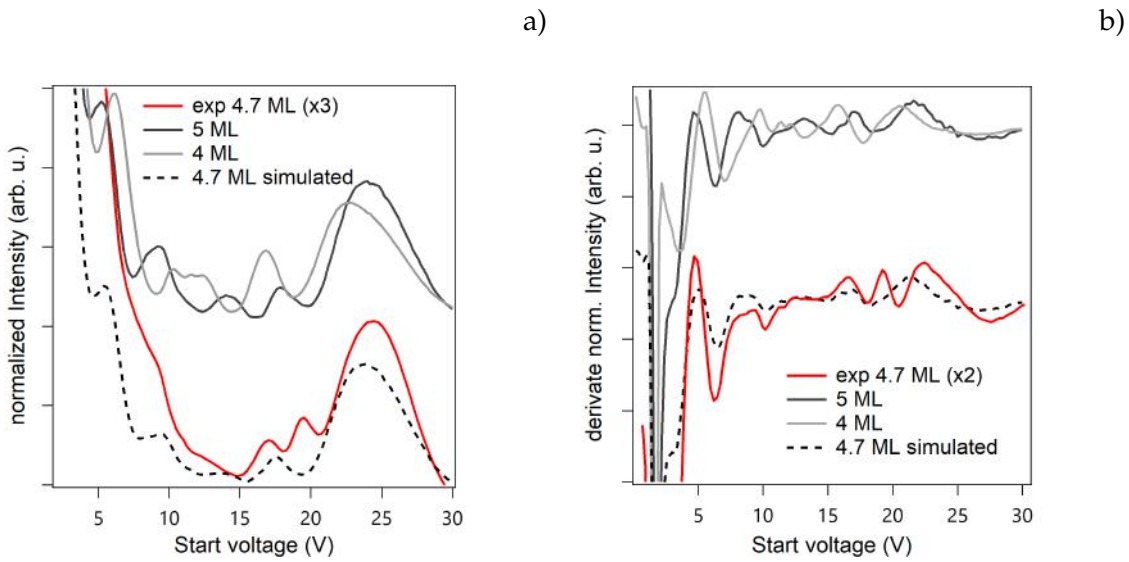

Figure 4.4: LEEM I-V spectra, Kinetic Energy from 0.2 to 30 eV, Field of View 10 µm, a) normalized LEEM I-V, b) derivative of normalized LEEM I-V.

and the simulated one are superimposed. The similarity between the experimental spectrum and the simulated spectrum can be noticed and may be considered a proof of the thickness of the cobalt layer.

In Figure 4.4 a) an additional peak at about 20 eV for the sample grown at room temperature is shown, instead, the simulated spectrum possesses only one peak. The additional Bragg peak was observed and interpreted due to the geometry of fcc stacking for several transition metals [30, 31] In this case the sample grown at room temperature shows the feature of *fcc* cobalt, instead the simulated spectra reveals *hcp* structure.

4.2.2 Graphene formation

Once the cobalt film was deposited on the Re surface, a single graphene overlayer was grown by the controlled decomposition of a carbon precursor, C_2H_4. The C_2H_4 molecules adsorb on the cobalt that plays both the role of a substrate and catalyst for the molecule decomposition. The sticking of the hydrocarbon is very low on the graphene covered surface. Thus as soon as the first layer is formed the rate of graphene formation drops significantly allowing the formation of a single layer graphene sheet [32].

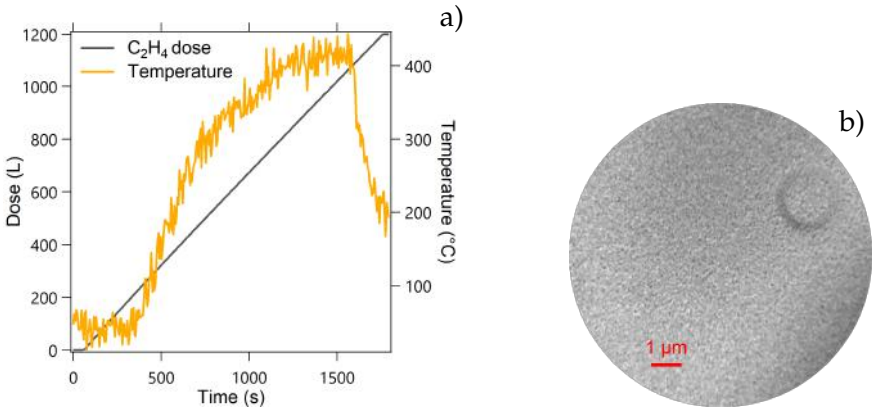

Figure 4.5: a) Gas dose and temperature plot showing the amount of C_2H_4 employed in the synthesis. b) LEEM image, acquired at 8 eV, field of view 10 µm, showing the surface completely covered by graphene.

C_2H_4 was added in the chamber at room temperature till the internal pressure stabilized at 10^{-8}mbar. The temperature was increased gradually up to $\sim$ 420 °C and the ethylene pressure was raised to $8{\cdot}10^{-7}$mbar and kept constant. The temperature was not raised any further to avoid the rupture of the Co film. A total C_2H_4 dose of 1200 L (L=10_6 Torr/s) was reached at the end of the growth. The temperature ramp and the gas dose can be seen in Figure 4.5 a).

In order to characterize the graphene overlayer, LEED and XPS analysis were performed. The former helps to determine the crystalline state of the surface, the latter the chemical quality of the graphene by looking at the C1*s* spectra. Note that, due to the similarity of primary diffraction spot positions of cobalt and epitaxial graphene, the two structures give rise to similar LEED patterns.

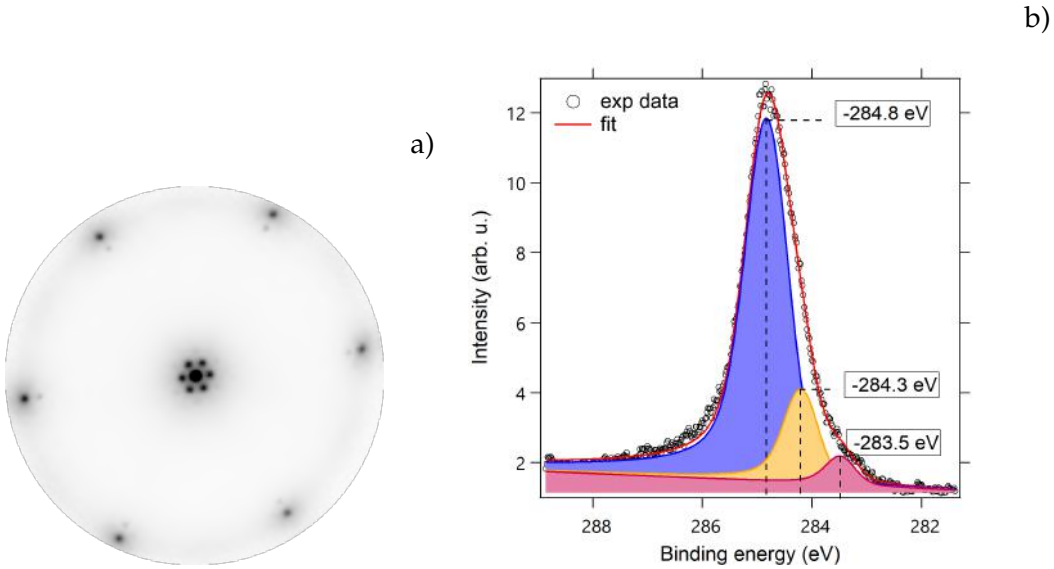

Figure 4.6: a) LEED image, acquired at room temperature at 60 eV. Reciprocal lattice of graphene and cobalt are observed and also a diffuse intensity at the same reciprocal distance. b) C *1s* spectrum of graphene layer, acquired at room temperature, at photon energy 400 eV. fitting using the DS model, in blue graphitic carbon, in yellow carbon atoms of defective graphene, in purple carbidic carbon.

The LEED pattern shown in Figure 4.6 a) reveals the presence of rotated graphene domains with respect to cobalt. In this case, a ring of LEED intensity is shown at the same reciprocal distance from the specular beam as expected of the graphene/cobalt spots. Thus graphene flakes with different azimuthal orientation coexist on the sample surface. In Figure 4.6 a) a Moirè pattern is also visible. The Moiré pattern may arise from the structural arrangement of the atoms or it is caused by interference process between scattered waves. This pattern derives from the mismatch between Co and Re, where for every 10 cobalt atom, there are 9 Re atoms leading to the 10×10 superstructure[33].

The XPS spectra analysis was performed at the C 1*s* core level of the graphene. The shape and the position of the spectrum in the binding energy allows to obtain information on the chemical environment of each carbon atom of the graphene layer. The fitting procedure, briefly explained in chapter 2.4.1, was followed resulting in the lineshape reported in Figure 4.6b).

The overall normalized C 1*s* intensity is consistent with a complete ML of graphene. The spectrum shows a broad peak which was fitted by three components. Each of the peaks is interpreted to correspond to carbon atoms in a different chemical environment. The main contribution arises from the curve at 284.8 eV. This should include two known carbon absorption sites within the graphene lattice: carbon on top of cobalt C_t, and in

the hollow between cobalt C_h. The curve at 284.3 eV should be referred to carbon coming from defective graphene and the shoulder at lower binding energy at 283.5 eV is due to the presence of carbidic species C_c on the surface possibly originating at the boundaries between graphene flakes or defective graphene[30, 34, 35].

The characterization of the sample assessed the composition of the stack with nominal thickness of $\sim$ 4.7 ML of cobalt deposited on Re. The graphene grown on cobalt can be considered as a complete single layer as a result of the analysis of XPS spectra and the LEEM image. However, the surface presents different azimuthal oriented graphene flakes. The sample grown by this procedure is called "$\mathbf{gr}_{dis}$" (disordered graphene) as labelled for further analysis.

4.3 Oxygen driven graphene growth

In this section another growth method for graphene was investigated. Prior to the graphene growth, we deposited the same 4.7 ML of cobalt on Re(0001) as in the previous section. The same characterization on the sample made sure that those 4.7 ML of cobalt had the same characteristics as the one in the previous section. This allows to focus on the differences between the graphene layers only. As it will be presented below, this growth method is performed while introducing in the chamber a small partial pressure of oxygen (O_2) in addition to ethylene in order to improve the graphene quality.

4.3.1 Graphene layer formation in O_2 atmosphere

In order to improve the structural quality of the graphene layer, a novel idea of adding a small amount of molecular oxygen was used during the CVD process. The intention in adding oxygen was to lower the graphene nucleation density and to increase the resulting graphene grain size at the relatively low temperatures used for the CVD process. It was observed that oxygen partial pressures of only a fraction of the C_2H_4 did not lead to the oxidation of cobalt, nor any oxygen signal was observed in XPS.

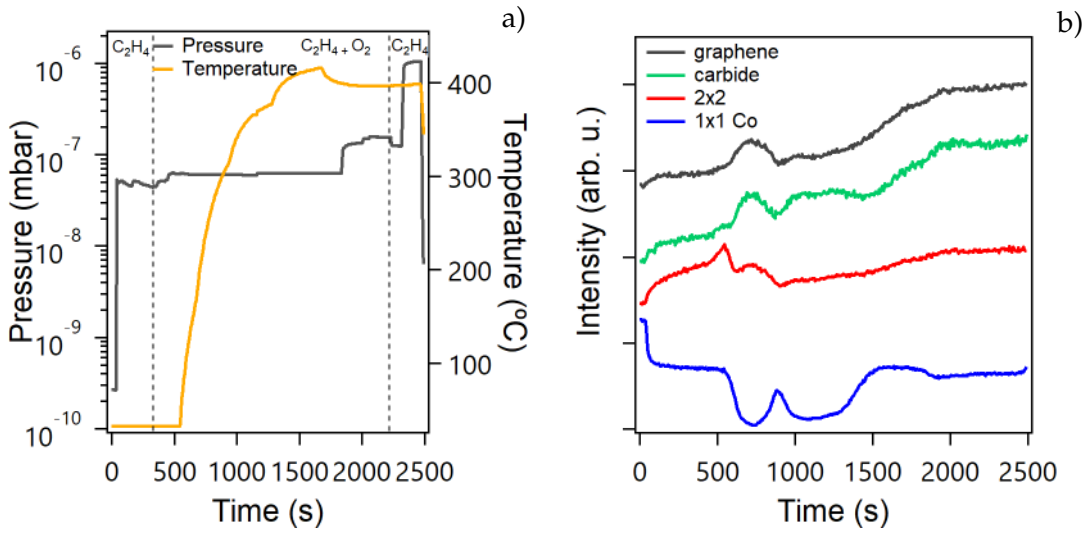

Figure 4.7: a) Temperature and total pressure of the growth chamber during the experiment. the dashed line, respectively indicates when the the oxygen was introduced on left and removed on right. b) Average LEED intensity as function of the time, electron energy 45 eV. "Graphene" refers to the diffuse diffraction ring corresponding to rotated graphene.

Similar to the previous graphene growth, the temperature ramp and gas pressures were carefully controlled. This can be seen in the plot in Figure 4.7 a). Initially, only ethylene was introduced in the chamber at $5{\cdot}10^{-8}$mbar. After about 5 minutes oxygen was introduced in the chamber until the total pressure reach $6{\cdot}10^{-8}$mbar giving an O_2 partial pressure of about $1{\cdot}10^{-8}$mbar. At this point the temperature was raised to about 400°C (temperature ramp 0.65 °C/s). During most of the growth the pressures were kept constant, while around 1800 seconds at 400°C the total pressure was set to $1.5{\cdot}10^{-7}$mbar by increasing the ethylene partial pressure, and at 2200 seconds oxygen was removed from the chamber. In order to complete the graphene coverage, the ethylene pressure was increased to 10^{-6}mbar.

During graphene growth the LEED intensities of spots were collected, and plotted as a function of time resulting in the graph in Figure4.7 b). Here each curve is associated with a different LEED spot during the growth. The images in Figure4.8, are the LEED

patterns taken at different times. Each of them highlights the structures observed during the graphene formation.

After the addition of oxygen, the 2×2 superstructures appeared in the LEED pattern Figure 4.8b) likely due to some oxygen ordered adsorption on cobalt [36]. The reciprocal unit cell is highlighted in red in Figure 4.8 b). Once the temperature exceeded 200 °C this superstructure disappeared.

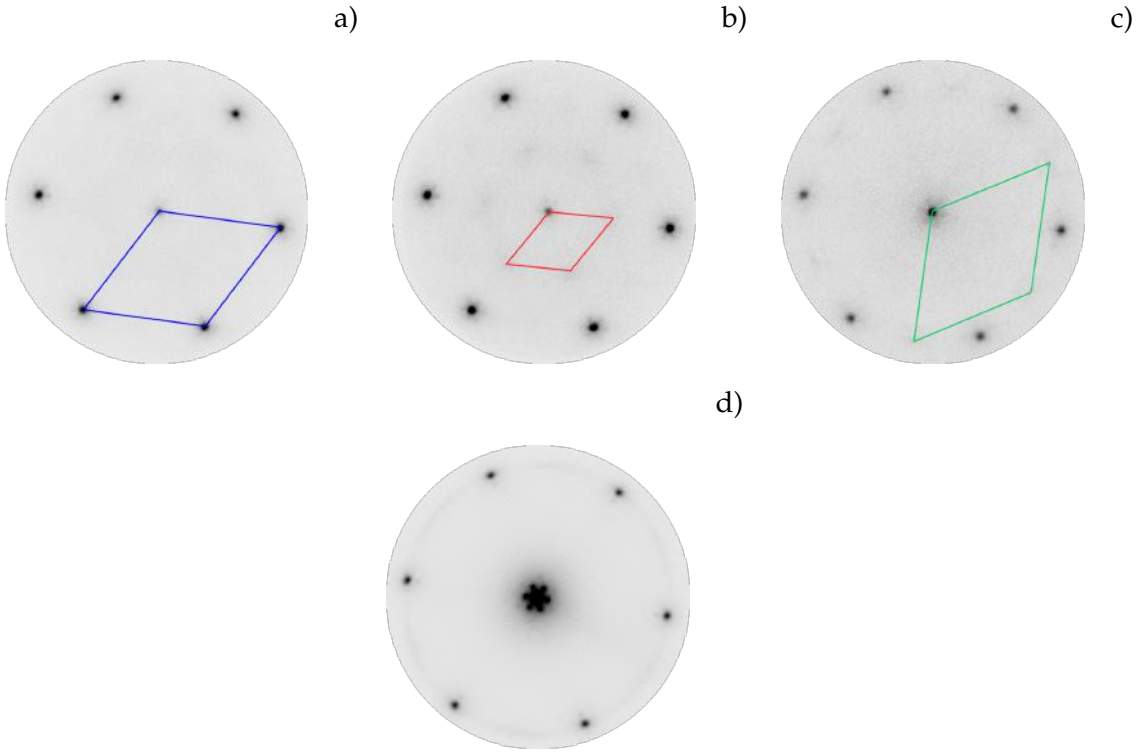

Figure 4.8: LEED images of graphene growth on cobalt surface, electron energy 45 eV; a) 1×1 structure of Co. b) 2×2 structure of oxygen molecules adsorbed on cobalt surface. c) Initial stages of graphene growth. d) Fully complete graphene layer along with the diffraction ring due to incoherent rotated graphene grains.

During the real time observation the 1×1 cobalt structure reduces in signal intensity Simultaneously diffraction spots from carbidic species arise in the LEED pattern as can be seen in Figure 4.8 c). These may be considered as the precursor for graphene formation [37]. The carbides on the surface dissolve above 250 °C. The spots from the carbidic species completely disappeared in the LEED pattern after 400 °C is reached.

From the observation of the LEED pattern dewetting of the Co film can be ruled out. This can be related to the surfactant property of C_2H_4 that prevent such dewetting, that is the rupture of flat film, it undergoes coalescence and form clusters. After 1200 seconds from the beginning of the growth the graphene starts forming. In the LEED pattern in Figure 4.8 d), both the 10×10 Moirè pattern and the diffraction ring became visible. This LEED pattern looks similar to the LEED pattern shown in Figure 4.6 a), i.e. the one of the rotationally incoherent graphene film of the previous growth. Therefore, we can conclude that also for growth in the presence of oxygen, the graphene layer is composed of both *epitaxial* and rotated units.

The quality of the graphene overlayer was assessed by LEEM and XPS in order to complete the characterization. The image in Figure 4.9 a) shows the surface of the sample after graphene formation. The image reveals a homogeneous surface with the presence of some granularity. The C 1*s* spectra in Figure 4.9 b) shows a broad peak and a small shoulder at lower binding energy. The spectra was fitted by three curves evaluating different con-

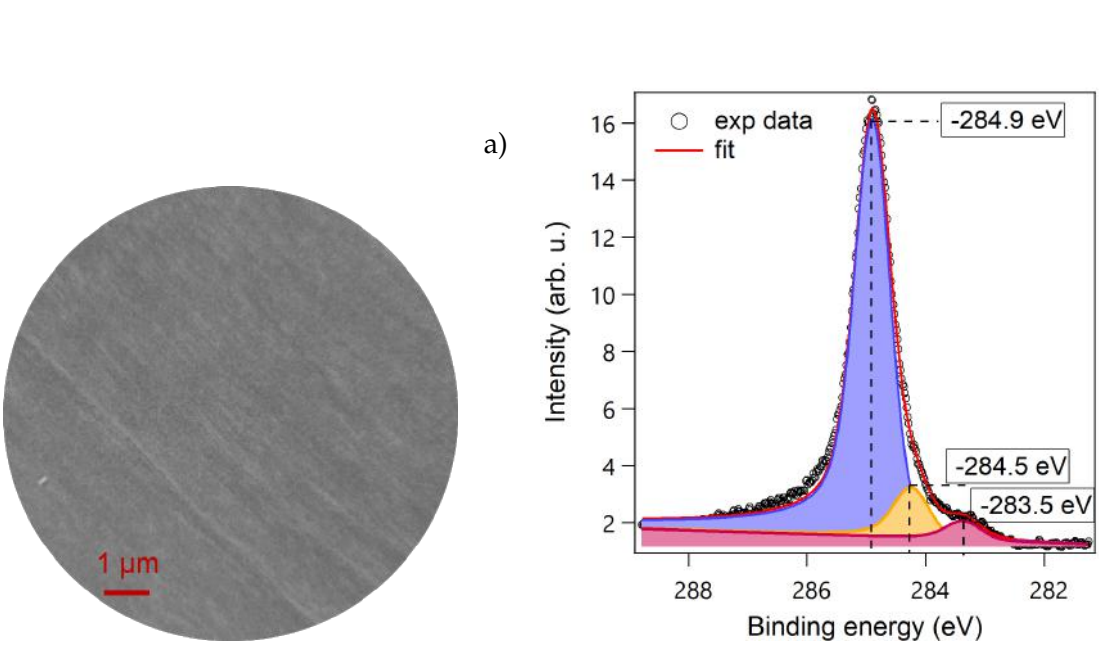

Figure 4.9: a) LEEM image of the graphene covered surface acquired at RT, field of view 10µm, electron energy 8 eV. b) C 1*s* XPS acquired at RT is shown along with the fit. Photon energy is 400 eV.

tributions as for the previous growth. The fitting method remains the same and also the considerations made before are unchanged. As before, the components C_t and C_h are fitted together in the blue curve centered at 284.9 eV binding energy. The component at 284.3 eV accounts for carbon atoms of defective graphene and the C_c at 283.3 eV for carbidic carbons. However, the overall XPS lineshape results narrower with respect to the one in section 4.2.2, shown in Figure 4.6b). Above all, the contribution from carbidic carbon seems to be reduced. This can be considered an improvement in the graphene quality, because most of the intensity is centred in the two sites related to graphitic carbon atoms [30, 38, 35].

Thus, we can conclude that the introduction of oxygen has led to a better graphene layer even though rotated domains are still present. This sample will be called "$\mathbf{gr}_{ox}$" as a label for further analysis.

4.4 Seeded Graphene growth and cobalt intercalation

The last idea employed for the synthesis of the graphene layer is to use the interaction between the Re(0001) substrate and carbon atoms, which induces epitaxial graphene growth [39]. After the graphene formation, the idea is to intercalate cobalt at the graphene-Re interface by thermal diffusion. This growth method will be divided into two parts. The first part involves an attempt to intercalate cobalt under a complete graphene layer. The second consists in the creation of small graphene islands on Re(0001), then intercalate 4.7 ML of cobalt, and finally complete the graphene layer by continuing the CVD process on the cobalt surface.

4.4.1 Cobalt intercalation under a complete graphene layer on Re(0001)

It is well known that graphene and rhenium interact strongly, and under high temperature conditions near 700 °C, only epitaxial growth takes place [40]. Importantly, the growth has to be done in short annealing cycles in order to limit the formation of carbides on the surface. This is done in C_2H_4 pressure near 10^{-7} mbar and fast heating-cooling cycles between 750 °C and 200 °C. In figure4.10 a) the time-dependence of temperature highlights the thermal cycles, where fast heating and slower cooling steps can be seen.

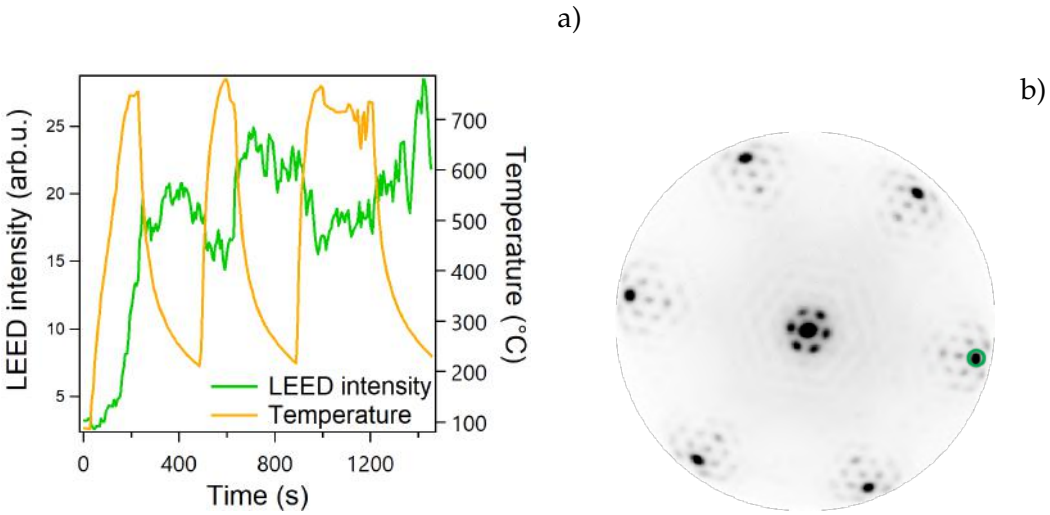

Figure 4.10: a) LEED spot intensity in green curve as a function of the time, superimposed to the temperature ramp, in yellow, employed during the growth. The spot analysed is highlighted on the LEED pattern with a green circle. b) LEED image of graphene on Re shows Moirè pattern associated with epitaxial graphene. Electron energy is 45 eV.

This procedure on the one hand limits the formation of carbides, and on the other, it avoids the bulk diffusion of the carbon atoms, which is favoured at elevated temperature. In Figure 4.10a) it can be appreciated that the intensity of the spot rises in the cooling part and decreases while heating the sample. This is due to the reordering of the surface as well as the Debye-Waller effect. The growth continues until the LEED pattern of the surface shows the formation of an extended Moirè as seen in Figure 4.10 b).

The appearance of the Moirè can be understood in terms of the spatial modulation of the graphene layer over the rhenium surface. The graphene unit cell differs with respect to the rhenium one, the difference is roughly the same as for cobalt and rhenium, so they have 10% of mismatch. This affects the graphene surface resulting in corrugated graphene sheet on the rhenium substrate [39].

In the next step cobalt was intercalated between graphene and Re. This procedure is well studied for other substrates such as Ir(111) [41]. Cobalt intercalation was done by 4.7 ML cobalt deposition at 250 °C over the graphene layer. The intercalation was assessed by LEEM, in Figure 4.11a), which shows the image of the surface after Co deposition. The surface appears homogeneous and seems to be covered by graphene without revealing cobalt. The slight variations in the intensity between the center and the outer part of the image is due to the different step morphology.

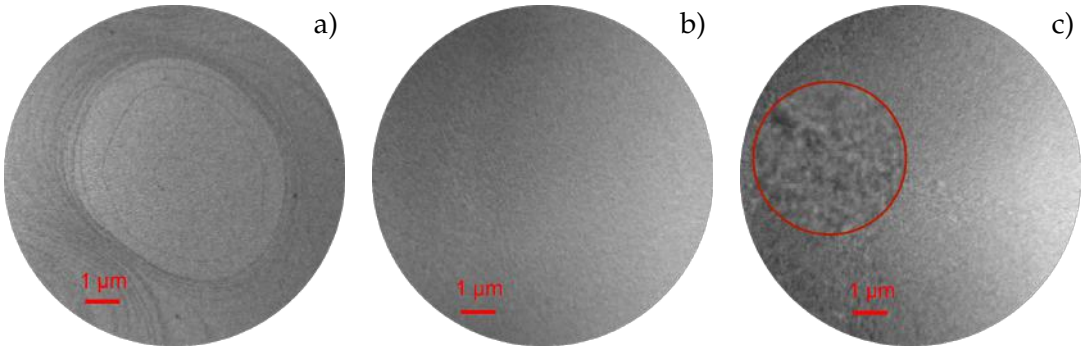

Figure 4.11: a) LEEM image acquired at RT, f.o.v. 10µm, kinetic energy 8 eV. b-c) XMCD image at Co L_3 edge (photon energy 780 eV), acquired at RT. b) Before annealing. c) After annealing.

In order to understand whether the intercalation was successful, XMCD imaging was used to visualize the magnetic domains on the surface. In this case, the XMCD-PEEM image at the Co L_3 edge does not show strong magnetic contrast, as can be seen in Figure 4.11 b) probably due to the small dimension of the domains with respect to the lateral resolution of the microscope. This is an indication that the intercalation did not result in a flat cobalt film uniformly intercalated under graphene.

To check whether the intercalation can be completed at higher temperatures, the sample was annealed at 410 °C for 5 minutes. Indeed in the previous cobalt growth experiments directly on Re(0001), the temperature for the first layer deposition usually is higher than 250 °C to obtain flatter films. The XMCD image after annealing is shown in Figure 4.11b). Here small domains are visible. The red circle in the image is a magnification of the image. From the image the magnetic contrast is evident, but is different with respect to previously grown Gr/Co/Re(0001) stacks. In short, the lack in reproducibility of the formation of magnetic domains with strong PMA can be seen as a hint of improper intercalation of cobalt.

LEEM image of the surface was taken at 40 eV and shown in Figure 4.12a). The image reveals the granularity of the film with small bright regions of about 60-100 nm in width. The presence of 3-D cobalt mesostructures likely contributes to this granularity and may have reduced the effective amount of cobalt in the flat part of the film, making it thinner than 4.7 ML. Another hint comes from the comparison between LEEM I-V spectra seen in Figure 4.12b). The two curves correspond to this sample and a previously grown graphene/Co/Re with 4.7 ML of Co. The disagreement between the spectra is another proof that the sample was properly not formed as a flat cobalt film under a graphene sheet.

Thus, a complete *epitaxial* graphene layer on Re(0001) does not allow the proper intercalation of Co, resulting in an inhomogeneous cobalt film under graphene. These affect the magnetic response of the system, that shows small magnetic domains with very low dichroic contrast.

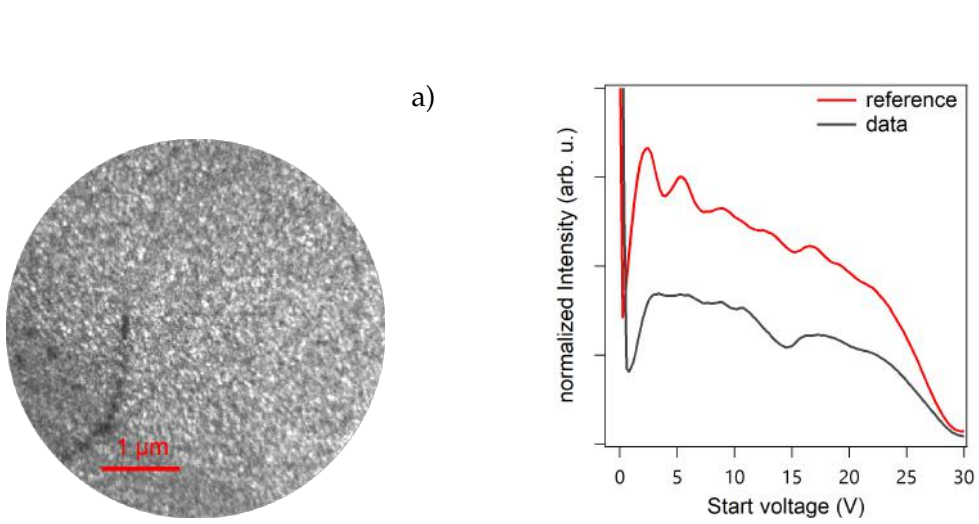

Figure 4.12: a) LEEM images acquired at RT, f.o.v. 10µm, kinetic energy 40 eV. b) Normalized LEEM I-V spectra, Kinetic Energy from -0.5 to 30 eV, Field of View 10 µm, two curves superimposed for comparison .image from the (01) position of the LEED pattern.

4.4.2 Stepwise Co intercalation on graphene/Re(0001)

As seen in the previous section, the complete *epitaxial* graphene layer on Re(0001) does not allow a proper Co intercalation. The problem of Co intercalation may derive from the lack of graphene defects that would facilitate intercalation. In order to overcome this difficulty, here we deposit an incomplete graphene layer on Re. The islands of the incomplete graphene will be intercalated by Co, and then used in a second growth stage as the nucleation points for the completion of the graphene layer on the intercalated Co thin film. Therefore, we first make sure to prepare an incomplete graphene layer on Re, monitoring the growth in LEED.

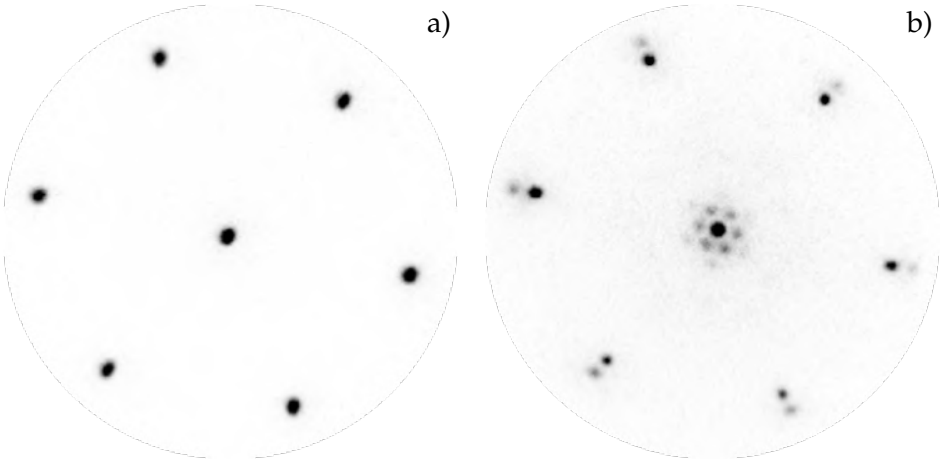

Figure 4.13: LEED pattern during graphene formation.The measurement was done at 45 eV electron energy. a) Re(0001) clean surface. b) The surface after the growth of graphene seeds.

The LEED pattern of the clean rhenium surface is shown in Figure 4.13 a), where only clean Re(0001) spots are visible. The graphene growth starts at RT, in UHV chamber the rhenium surface was exposed at $5{\cdot}10^{-7}$ mbar of C_2H_4 for about 15 minutes, which correspond to about 385 L of C_2H_4.

During real time observations, it was noticed a lowering in the intensity of the diffraction spots ascribed to Re as seen in Figure 4.13a), while the first graphene seeds are formed. The Moirè pattern between graphene and Re shown in Figure reffig:grafig1 b) indicates the epitaxial growth of graphene. The pressure of C_2H_4 is reduced when the second order Moirè spots starts becoming visible in the LEED pattern in Figure4.13 b). After recovering the pressure to low 10^{-9} mbar range, the annealing is turned down and the sample is brought to room temperature. This procedure leads to the formation of graphene seeds with small lateral extension on the rhenium surface.

As it was mentioned above, the second stage of the growth consists in the deposition of cobalt over the rhenium surface partially covered by graphene. The parameters for the deposition are the same as utilized in the other growth, but the temperature was fixed at 250 °C. This provides sufficient thermal energy to cobalt atoms for intercalation. The deposition was followed by LEED looking at the decrease in the Moirè pattern intensity and the eventual increase in the intensity of the spots due to the formation of graphene/cobalt.

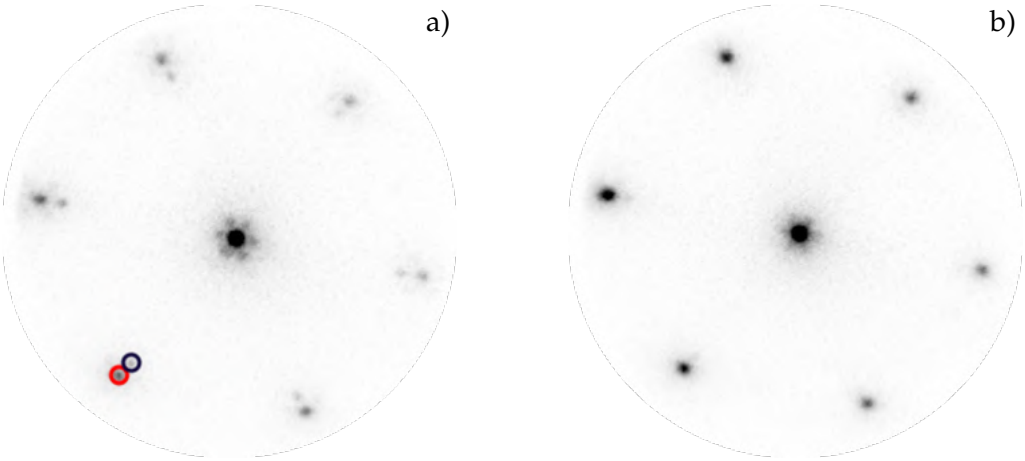

Figure 4.14: The evolution of the LEED pattern during graphene formation and Co deposition. The measurement was done at 45 eV electron energy. a) Re(0001) surface after graphene seeds growth acquired at RT. b) LEED pattern of the surface after cobalt intercalation.

The LEED pattern in Figure4.14 a) represents the surface structure at the beginning of cobalt deposition. It shows the same LEED pattern as in Figure 4.13b) but acquired at a different temperature. As already mentioned, during Co deposition the Moirè intensity drops as for the intensity of the Re spots. This can be seen in Figure 4.14a), in which the red circle highlights the diffraction spot from cobalt, while the blue one is referred to rhenium. At the end of the deposition, the spot in the blue circle position disappears and the other spots increase in intensity.

The graphene layer on top of the intercalated Co film was completed by CVD process using ethylene in a similar fashion as in the previous sections. The temperature was around 400°C avoiding the rupture of the film. The surface of the sample after the graphene completion appears homogeneous as can be noticed in Figure 4.15 a). To check the crystalline structure of the surface a LEED pattern was taken, and it is shown in Figure 4.15 b). In this pattern, all the spots originate from the superimposition of graphene and cobalt reciprocal lattices. Interestingly it is the diffraction ring is absent, which indicates that the graphene is mostly *epitaxial*.

The chemical analysis of the resulting surface was done by measuring C 1*s* spectra as seen in Figure 4.15 c). The lineshape was fitted again by three curves in order to be consistent with the analysis done for the previous methods. The usual three contributions are observed from different carbon species. As before the greater contribution in the curve

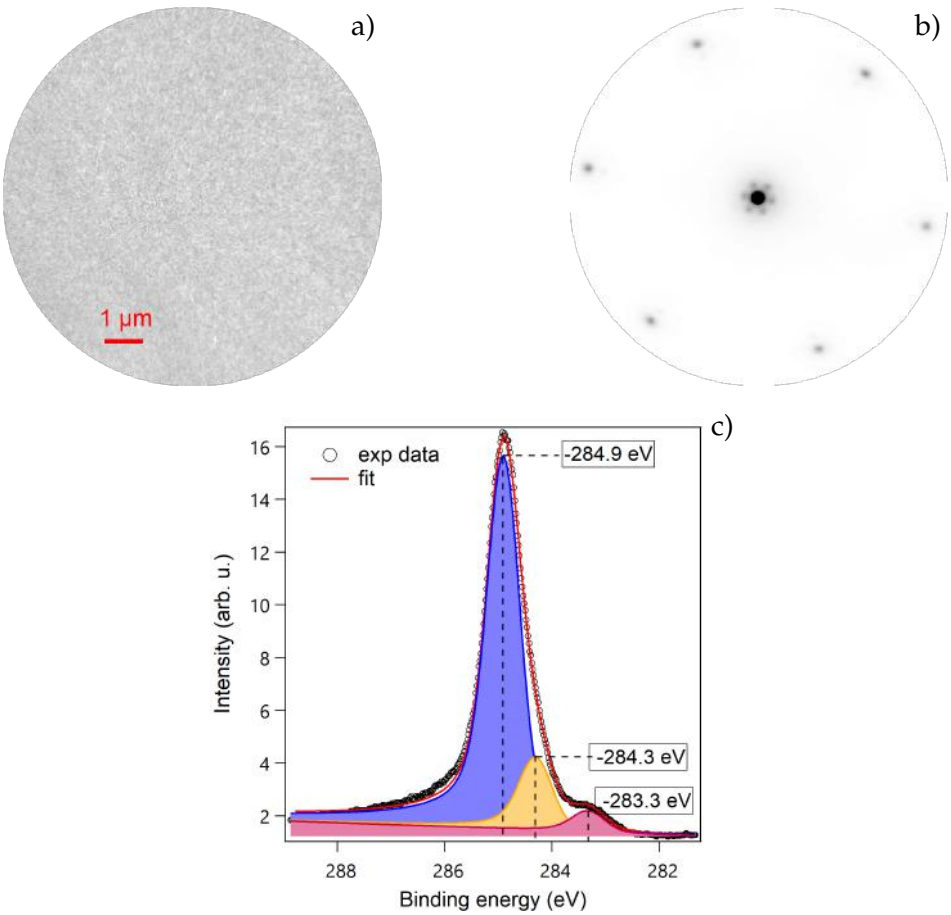

Figure 4.15: a) LEEM image of the surface after graphene layer completion. Acquired at RT, f.o.v. 10µm, kinetic energy 8 eV. b) C 1*s* XPS spectra, acquired at RT, photon energy 400 eV.

at 284.9 eV arises from C_t and C_h carbon absorption sites. The curve at 284.5 eV is refereed to carbon atoms of defective graphene flakes C_d, and the carbidic contribution C_c at 283.5 eV. However both C_c and C_d contributions are smaller with respect to C_t and C_h.

In summary, the film obtained in this manner appears homogeneous in LEEM and it seems composed only by single orientation graphene according to the LEED pattern. Due to well defined *epitaxial* growth, the graphene grown in this way will be called "gr_{epi}" (epitaxial graphene) for further analysis.

4.4.3 Seed dimension evaluation

The success of the seeded graphene growth on Co move the attention on two key parameters: seeds lateral dimension and surface density of these nucleation points on rhenium. Via a spot-profile analysis in LEED, it is possible to estimate the dimension of graphene flakes. In addition to the LEED spot analysis, XPS was performed. The first gives us information on the lateral extension of graphene seeds, the second allows us in order to roughly determine the graphene coverage of the surface.

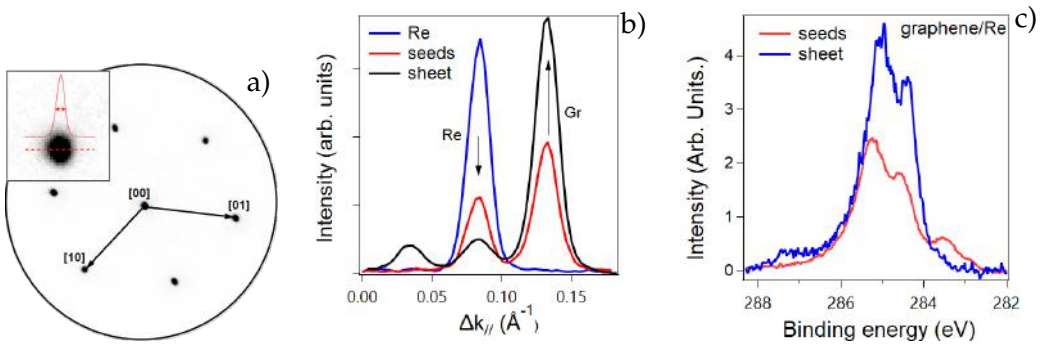

Figure 4.16: Characterization of graphene seeds. a) LEED snapshot of graphene growth on Re, the image was taken during the growth of the seed. The red line indicates the section of the profile take into account for the analysis. Electron energy is 45 eV. b) LEED spot profile analysis, the blue line represents the profile of bulk Re, the red line is the profile of the spot at the end of the growth of the seed, the black line represents the Moirè pattern formed after complete formation of graphene sheet on Re. c) XPS spectra acquired at room temperature, photon energy 400 eV: C 1 1*S* of graphene on Re(0001), the spectra in red line are related to graphene seeds, the blue curve depict spectra of a complete graphene layer on Re.

The information on the dimension of graphene domains formed on Re(0001) as well as the assessment of the proper formation processes, are obtained by LEED. The evolution of the system is followed by looking at the diffraction spots. In the first stage, only the signal from bulk Re are visible. Then after C_2H_4 exposure ($\sim$ 400 L) and heating-cooling cycles, spots from graphene arise. The profile of the intensities of the diffraction spots from the real time acquisition in LEED is taken along the line that connects the (00) spot to the first order spots as can be seen in the snapshot in Figure 4.16 a).

Collecting profiles at a different time of the growth, the graph in Figure4.16 b) was obtained. The blue curve is is taken from the clean Re(0001) surface and it is useful for the evaluation of the transfer width, of the instrument. In other words, for a single crystal metal with large terraces, the width of this spot reflects solely the instrumental broadening. The red curve in Figure 4.16 b) instead is taken after the formation of the seeds, while the black curve is the profile associated with a complete sheet of graphene on rhenium surface. The additional peak in the black curve is related to the structural modulation between Re and graphene resulting in the Moirè pattern in Figure 4.10 b).

The curves in Figure 4.16 b) were fitted by Gaussian functions and the value of full width at half maximum (FWHM) was used for an approximate evaluation of the dimensions of the seed. The instrumental broadening from the FWHM of the Re spots was taken into account when calculating the reciprocal of the FWHM from graphene spots. This analysis gives a value between 3 to 4 nm as the lateral extension of the seeds. Dimension of the graphene flakes in the complete sheet was instead between 5 to 7 nm.

The approximate value of the graphene coverage is given by XPS spectra shown in Figure 4.16 c), where it can be seen that the two C 1*s* spectrum superimposed appear similar. The lineshape possesses two main components related to different absorption sites, one strongly interacting and the other less interacting [39]. The red curve shows an

additional peak at around 283.5 eV which is due to carbidic species on the Re surface, they could be the carbon atoms at the boundaries of the graphene seeds. The ratio between the integral of the signals is proportional to the relative amount of carbon atoms. This allows to estimate the coverage of the graphene seeds between 30% and 50% of the Re surface. From this result combined with the value obtained from LEED. The estimated distance between adjacent graphene seeds is around 3 to 5 nm, which is enough space for cobalt atoms to intercalate properly. In addition should be noted that the graphene seeds are near enough to prevent the film rupture during the cobalt deposition and the subsequent CVD process at high temperature.

4.5 Comparison of growth methods

4.5.1 LEED analysis

The formation of the graphene layer and its quality are confirmed by looking at the LEED pattern evolution, for each growth method selected. The comparison based on LEED patterns is focused on the intensities between adjacent spots. The presence of a signal along the diffraction ring corresponding to graphene lattice constant means that graphene flakes on the surface are present with multiple orientations. Conversely if the signal is concentrated on the spots, it means *epitaxial* graphene grown on the substrate.

Three LEED patterns collected on different samples were taken at the same kinetic energy for better comparison. Due to different setup conditions between the measurements the patterns may vary. In order to eliminate these differences, I convert pixels in degrees. The hexagonal structure of graphene allows easily to select the reciprocal space between spots and convert it in degrees, concerning the angle spanned by adjacent spots is 60°.

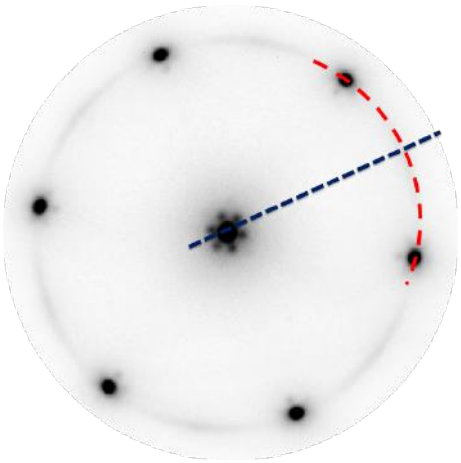

Figure 4.17: Representation of the profile taken for the analysis. The red dashed line is the ark of a circumference, which is perpendicularly by the dashed blue line.

The way in which the intensities are extracted is explained in Figure 4.17 were the red dashed line is the arc and the blue one is the cut perpendicular to the arc. Both profiles are normalized, the first using the background intensity around the arc and the principal spots, the latter by the intensity of the (00) spot of the profile.

Collecting the arc and the cut profiles for the three LEED patterns from the three growth methods, the plots reported in Figure 4.18 are obtained. The plot in Figure 4.18 a) represents the intensities along with the arc.

Despite the noise, the main difference is the intensity between the two peaks. From the image 4.18 a) this intensity corresponding to the diffraction ring seems to be present only

in the graphene grown in oxygen and the disordered one, i.e. gr_{ox} and gr_{dis} respectively. In fact for these two cases, in the final LEED pattern a blurry diffraction ring is present, signifying the presence of multiple orientations of the graphene flakes. However, most of the sample can be considered *epitaxial* with respect to the underlying cobalt layers.

The sample called gr_{epi} instead does not present any signal intensity in the same region as it can be seen in the blue line in figure 4.18 a). Therefore, the surface of the probed area results in single orientation graphene flakes matching the hexagonal structure of Co. For better appreciating the difference between samples a profile perpendicular to the arc at about 30° was taken for each LEED patterns as shown in figure 4.18b). It confirms the presence of different graphene grains orientation in the sample gr_{ox} and the sample gr_{dis}, but zero for the sample gr_{epi}.

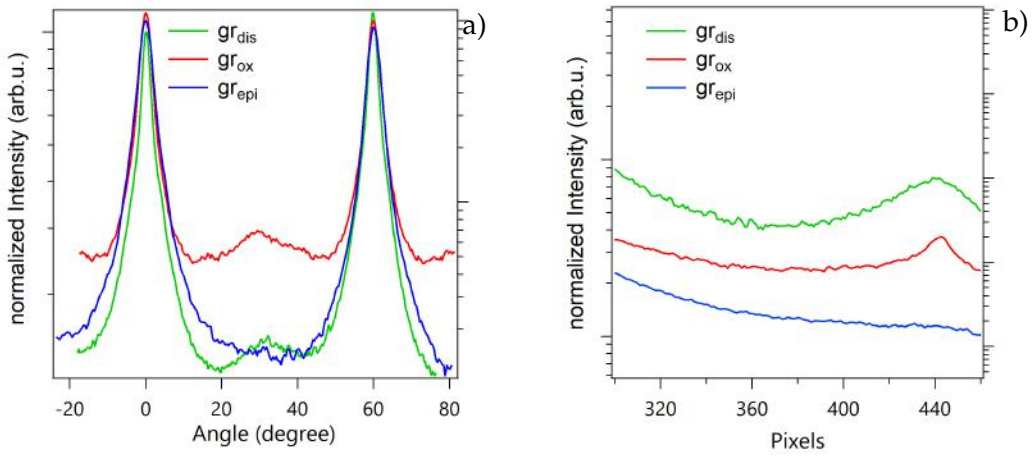

Figure 4.18: a) Arc profiles from three LEED pattern, the distance in the image is converted in degree. b) Cut profiles of the same LEED pattern.

From the profiles in figure 4.18 b) it can be seen that the domain size of the rotated flakes for gr_{dis} is small due to the broad intensity, since the width of the profile is inversely proportional the grain size.

The opposite is seen for graphene grown in the presence of oxygen that presents a sharper profile with respect to the other sample. This means that the rotated graphene flakes as scattering units give diffraction signal are similar in dimension and bigger with respect to the rotated flakes of gr_{dis}.

4.5.2 XPS analysis

Besides the differences within the samples grown by alternative procedures, the chemical state of the graphene layer is a fundamental parameter. Here the C 1*s* spectra from the three methods are collected and plotted together for better comparison.

The plots shown in the previous sections (4.2.2, 4.3.1, 4.4.2) are reproduced in figure 4.18 b). Displaying them together allows to see the pronounced differences in the lineshape. The red and blue curves in Figure 4.19, for gr_{ox} and gr_{epi} appear identical, and the small differences have to be ascribed to the different settings during the acquisition. The big difference is gr_dis. Both the intensity and shape of the gr_dis is lower due to a slightly lower carbon coverage.

The curves in red and blue in Figure 4.19 corresponding respectively to gr_{ox} and gr_{epi} look equal. This means that chemically the sample called gr_{ox} in red and gr_{epi} in blue are identical. This is because both samples are composed of several small flakes of graphitic carbon atoms, so they are not an ideal infinite surface. They present several boundaries

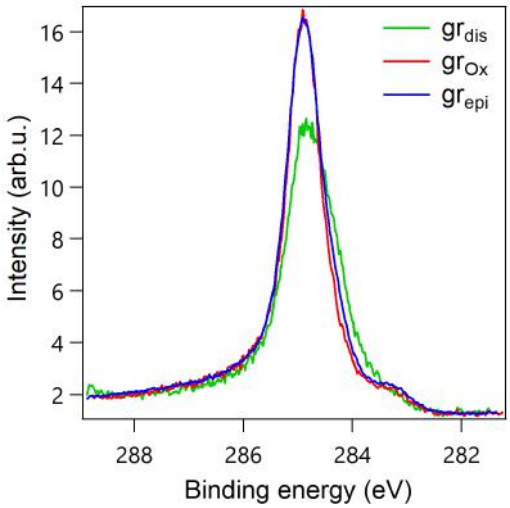

Figure 4.19: C1s XPS spectra of the three samples, photon energy: 400 eV. The spectra were acquired at RT.

with carbon atoms bonded to cobalt surface, leading to the formation of carbidic species as can the seen in both the spectra around 283.5 eV. The level of disorder on the surface causes the overall broadening of the lineshape.

While for the sample called gr$_{epi}$ it is not clear how the growth proceeds because it is similar to the one that produces gr$_{dis}$. The only difference is in the preexisting nucleation points, that may have driven the final reaction discouraging the formation of other rotational domains in the sample. This may have favoured a favourable exposure to carbon atom resulting in higher coverage.

Chapter 5

Magnetic properties of Gr/Co/Re(0001)

The last part of the thesis is focused on the magnetic properties of the samples explained in section 4.1. The main motivation is the influence of the growth method and the graphene quality on the magnetism of cobalt. As it will explained in this chapter, this is achieved by characterizing the sample by XMCD and MOKE.

In agreement with works in the literature, the presence of graphene overlayer on cobalt induces perpendicular magnetic anisotropy (PMA). Thus, the Spin Reorientation Transition (SRT) of Co/Re(0001), which takes place at 3-4 ML in uncovered Co ultrathin films, moves to higher thickness values for graphene/Co [42, 43]. Importantly, the MOKE analysis reveals that the structural properties of graphene sheet have an effect on the coercive field as well as the temperature-dependent saturation magnetization. In particular, epitaxial graphene on top of cobalt has a higher coercive field at all temperatures with respect to the sample composed by multiple azimuthal orientations of graphene.

5.1 Magnetism in thin films

Magnetic materials are usually determined according to their long range magnetic order. The most typical classes of magnetic systems with spontaneous long-range order are ferromagnets, antiferromagnets, and ferrimagnets. Paramagnetic and diamagnetic materials do not show any long-range order in the absence of an external field. In ferromagnetic materials, which are relevant for this study, all magnetic moments are ordered parallel to each other below their ordering temperature, termed as the Curie temperature (T_C). At room temperature, only few elemental materials are ferromagnetic i.e. they have Curie temperature greater than RT, which are the 3d metals Fe, Co and Ni, along with the 4f metal Gd. As it has been explained in detail in the previous chapter, cobalt in ultrathin film form is the focus of this thesis.

The magnetic anisotropy (MA) is a fundamental property of a magnetic material, which not only determines the preferential direction of magnetization but also its stability [44]. The main mechanisms responsible for MA are: the magnetocrystalline anisotropy, the shape anisotropy and the magneto-elastic anisotropy. the Magnetocrystalline anisotropy arises from the spin-orbit interaction, where the crystallographic arrangement strongly determines the alignment of atomic orbitals and thus creating a tendency of spins to align along particular axes via spin-orbit interaction. Instead, the shape anisotropy is a magnetostatic phenomenon, thus the magnetization vector will lie in the direction that minimizes the stray magnetic fields outside the sample [45, 46]. Magneto-elastic or strain anisotropy is based on the magnetostriction effect, which relates the strains to MA.

Thin films are different compared to the bulk materials due to the presence of the surface and interface. The broken in-plane vs out-of-plane symmetry in thin films may result in additional MA contributions. One of these can be based on magneto-elastic interactions due to interfacial strain effects. Another is based on an electronic rearrangement at the interface or surface along with spin orbit coupling. There is also the dipolar contribution that in thin films it is known to force the magnetization in plane in order to minimize the stray magnetic fields outside the material [44, 47] .

In order to assess the influence of graphene-cobalt interface on the MA, is focused on the two chemically equivalent and structurally different samples gr_{ox} and gr_{epi}. In this way the connection between the crystalline structure of the sample and its magnetic properties can be singled out.

5.2 Magnetic domain morphology: XMCD study

The magnetic domain morphology and size are visualized by XMCD-PEEM imaging. The contrast levels and the shape of the magnetic domains lead to the evaluation of the magnetization direction. The XMCD effect is proportional to the magnetic moments that are parallel to the light direction. Thus 16° grazing incident direction of the setup leads to higher sensitivity to in plane magnetization. However, it is still possible to detect out of plane magnetization with reduced sensitivity by a factor of down to a quarter of the total signal.

All XMCD images were acquired at room temperature. The photon energy was 780 eV matching the Co L_3 absorption edge. The effect of the acquisition geometry can be seen in Figure 5.1 a), where the contrast in the image is distributed in a grayscale. The small spots that appear black and white (with higher contrast) are due to regions where the magnetic moments are lying in the surface plane with a larger component along the beam direction. Possibly, these are cobalt clusters with larger thickness with respect to the overall film, as for thicker cobalt the magnetization turns in-plane.

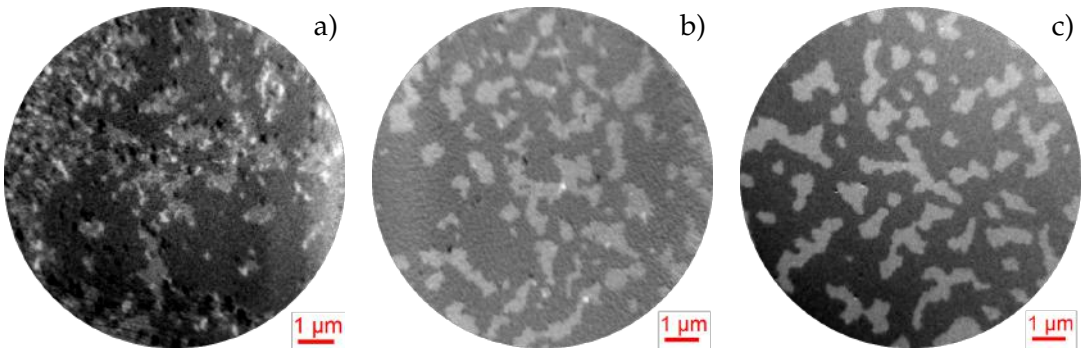

Figure 5.1: XMCD Images acquired at R.T. at Co L_3 edge, photon energy 780 eV. Images from three different samples of graphene/Co/Re multistack. a) gr_{dis}. b) gr_{ox}. c) gr_{epi}.

The sample surface pictured in Figure 5.1 a) comes from the sample called gr_{dis}. The sample presents rotated graphene domains with respect to the cobalt surface, and it was grown by a direct CVD process. The thicker cobalt regions may derive from the annealing procedure. The defective graphene of the sample gr_{dis} in the same image in Figure5.1 a) could have not stabilized enough the cobalt film, that makes clusters as the temperature increase.

The large dark and the bright areas with a lower level of contrast concerning the other regions are related to magnetic domains with magnetization direction out-of-plane. The out of plane magnetic domains appear fragmented with a lateral dimension of hundreds of nm. The domain walls are not defined and there is clear coexistence of in-plane and out-of-plane magnetization.

As for the sample gr_{dis}, gr_{ox} presents multiple orientations of graphene flakes over the cobalt surface. The rotated crystallites, however, seem to be larger with respect to gr_{dis} sample. From XPS the graphene layer seems more complete with respect to the gr_{dis} as noticed in the chapter4.5.2. The magnetic domains of the sample gr_{ox} are shown in Figure5.1 b). Even in this sample, small spots with higher level of contrast are regions where the magnetization lies in plane. These are ascribed to thicker cobalt clusters, as in the previous sample. However, there are fewer in plane domains. Most of the surface shows a single contrast due to out-of-plane domains. The domain size is not homogeneous, varying from tens to hundreds of nm. The morphology of the boundary of the domain is not well defined.

The last sample gr_{epi} should be composed only by *epitaxial* graphene. The amount of carbon atoms on the surface is comparable to the previous sample gr_{ox}. In this sample only one level of contrast is seen as can be noticed in Figure 5.1 c). No in plane domains are visible. The domains of this sample appear well defined with a lateral dimension of hundreds of nm, similar result can be found in literature [48]. From the images in Figure 5.1 c), the sample gr_{epi} possesses higher ratio of bright over dark regions with respect to the other two samples. This sample shows the strongest PMA and there is no presence of regions with in-plane magnetization.

The last two samples were studied in detail by looking at the behaviour of the magnetization vector in the presence of an applied magnetic field. These two samples differ in the crystalline structure but are identical in their chemical state. The sample gr_{dis} was not taken into account because it is different from the others both chemically and crystallographically. Thus a correct comparison could not be possible because it would be difficult to decouple crystal structure and chemical state from the magnetic anisotropy.

5.3 Magnetic anisotropy, MOKE

The samples were illuminated by linear polarized light from a laser source while immersed in a variable field. The light reflected from the sample was collected and the signal was plotted as a function of the applied magnetic field. The result is a hysteresis loop where the important values are coercive field and remanence. The former is the field to be applied to bring the magnetization from a certain value to zero. The remanence is the residual magnetization when the applied field is zero.

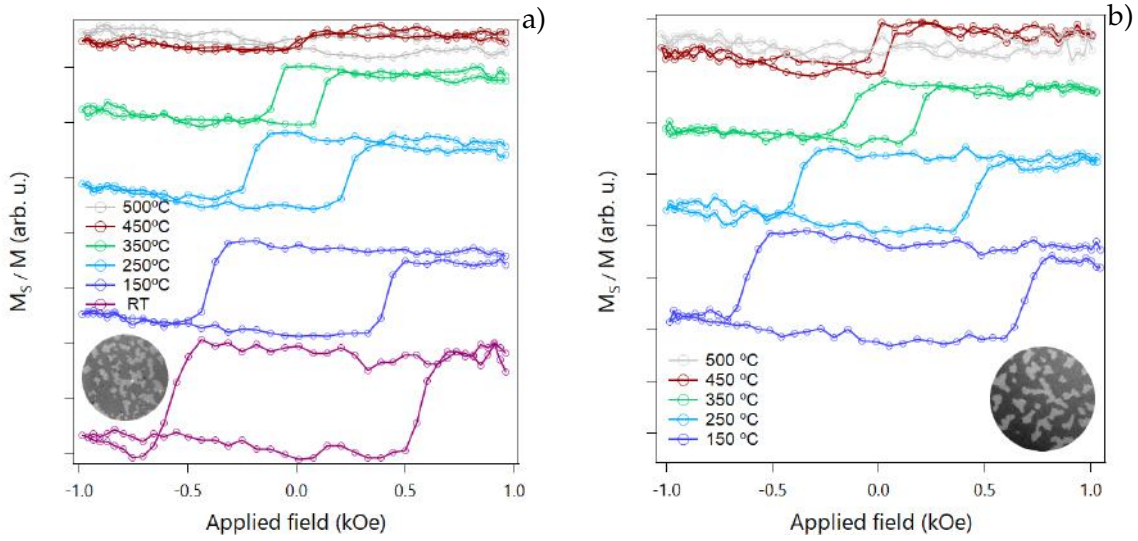

Figure 5.2: Polar MOKE response for graphene/Co/Re acquired at various temperature. Laser wavelength 632.9 nm a) gr_{ox}. b) gr_{epi}.

The setup allows to perform measurements at different temperatures. This feature was exploited to find the Curie temperature for these graphene/Co thin film. The temperature is increased starting from room temperature until the magnetic signal vanishes. The plots also display the XMCD image of the corresponding surface.

The two samples selected gr_{ox} and gr_{epi} show PMA, thus the MOKE polar configuration was chosen. Hysteresis loops are recorded every 50°C interval. The loops in Figure5.3 a) were obtained from the sample gr_{ox}. The sample reached the temperature of 400°C before starting to lose the magnetization. The measurement at 450°C still shows weak magnetic signal, while the measurement at 500°C is pure noise. The Curie temperature for 4.7 ML of cobalt lies between 400 and 500 °C, while for bulk cobalt is more than 1000°C. The square shape of the loops follows similar behaviour and it is lost at a higher temperature. The magnetic signal and both remanence and coercive field decrease, with the increasing temperature of the sample.

The same measurements were done for the sample gr_{epi},shown in Figure 5.2 b). The same temperature interval and steps were chosen. The measurement at room temperature is not shown because it was not possible to reach the saturation field. The applied field was not strong enough to obtain a loop. This sample shows square magnetic hysteresis even at 450°C and, as for the sample gr_{ox} the measurement at 500°C is pure noise. In this case, seems that the Curie temperature is shifted at slightly higher temperature between 450°C and 500°C.

The coercive field and the remanence for the two sample are plotted as a function of the temperature as seen in Figure 5.3. Here the points for each temperature steps are collected. In the Figure 5.3 a) is shown the coercive field for gr_{ox} in red and for gr_{epi} in blue. Both

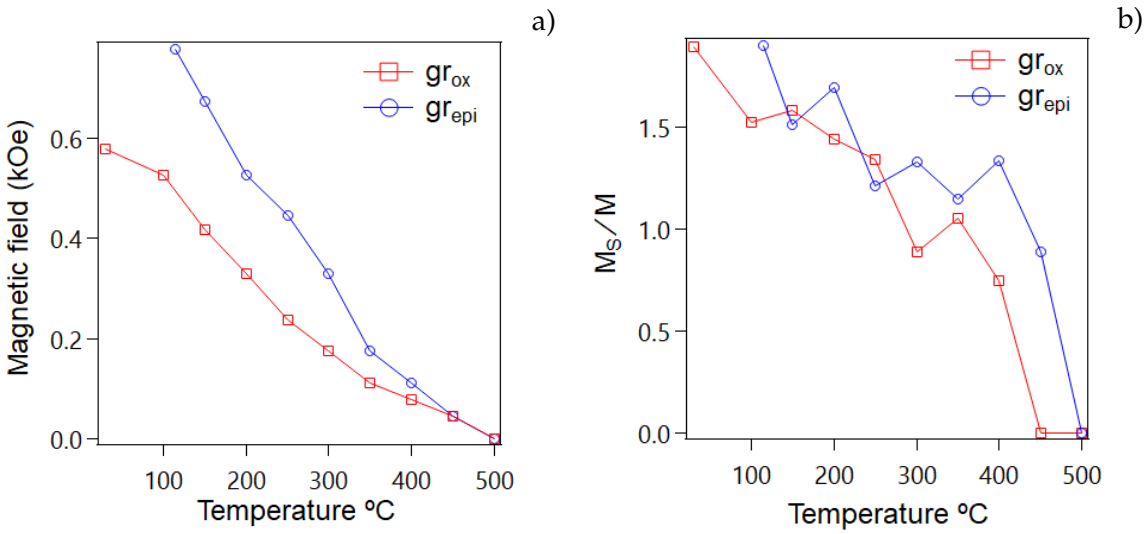

Figure 5.3: Summary of the data points acquired in the hysteresis loop. Red curve/dots gr_{ox}, blue curve/dots gr_{epi} a) Coercive field. b) Remanence.

decrease as the temperature increases. They reach about the same value at 450°C and go to zero at 500°C. The other points show that the sample gr_{epi} possesses higher coercive field at every temperature making it a stronger magnet.

The remanence for the two samples are plotted in Figure 5.3 b). The remanence of the sample gr_{ox} decreases as the temperature is increased and it drops near zero value, approaching the Curie temperature. The sample gr_{epi} instead shows a similar decrease but at 450°C it still shows a value different from zero of the residual magnetization. Both samples go to zero value of remanence as the temperature reaches 500°C.

The difference in these sample lies in the different spatial orientation of the graphene units over cobalt surface. The XMCD images show similar magnetic domains over the sample surface. Both samples show domains with out of plane magnetization. However the sample gr_{epi} appears more homogeneous, looking at the domain morphology and size. On the other hand, as reported here, the measurements obtained with the MOKE setup instead reveal a clear difference between the samples. The coercive field for the sample gr_{epi} is larger with respect to the sample gr_{ox}. It is also more stable with respect to the high temperature [49]. It maintains the magnetic signal at 450°C and even the remanence lasts longer with respect to the sample gr_{ox}.

These can be considered hints of the influence of the structure of the graphene overlayer on the magnetic response of the cobalt thin film. The two samples appear identical from the chemical point of view, in the frame of the resolution of the instrument. Therefore, it can be concluded that the *epitaxy* of the graphene in the sample gr_{epi} improves the magnetic response of the metal film.

Chapter 6

Conclusion

In this work different pathways for the formation of a single graphene layer were tried. The aim was to obtain high quality graphene/Co/Re(0001) stack system. The main difference among the samples is the graphene quality and its growth method. The interaction between metal surfaces and carbon atoms was exploited, to induce preferential orientation in the resulting graphene sheets.

The reactivity of the growth process was modified by introducing molecular oxygen and was seen to influence the final graphene quality. The homogeneity of the thin film, the orientation and the quality of graphene single layer were assessed by different techniques: LEEM, LEED for direct and reciprocal imaging of the surface, obtaining information on the surface (presence of defects or not) and its crystalline structure respectively. Chemical analysis was performed by XPS spectroscopy that allows to discriminate between allotropes of carbon.

The other important part of the thesis was the study of the magnetic response of these systems. Images of the magnetic domains were obtained by XMCD-XPEEM and hysteresis loop associated to each sample was collected by MOKE. All the samples which without graphene are expected to have in-plane magnetization revealed the presence of out-of-plane magnetization. This demonstrates the presence of PMA and it means that the interfacial interaction between Co and graphene plays a fundamental role in the magnetic properties of the system.

Even if the XMCD images do not allow to observe appreciable differences among samples, the hysteresis loops, showed that gr_{epi} has stronger PMA with respect to the others. The last growth method is a good candidate for further experiments leading to only *epitaxial* graphene. Starting from these results the possible outlook of this thesis could be multiple:

- Systematically change the ferromagnetic material with other 3d metals, or more complex alloys or oxides in order to check if the growth method can be applied to a wider range of materials.

- Change of the substrate because as for the graphene layer on top, it influences the electronic structure of Co and its magnetism.

- Use other ferromagnetic metals on top of graphene/Co to verify the magnetic coupling that take place in presence oF graphene.

- Substitute if possible the Graphene with other 2D materials as Boron nitride, Phosphorene and Transition Metal Dichalcogenides.

- Obtain a procedure for the formation of multiple graphene layerS with high ordered spatial orientation and subsequently study the effect of thicker graphene spacers on the coupling between adjacent ferromagnetic materials.

Acknowledgements

I should thank many people for this work, but I will concentrate only on who took part actively. First I have to thank my supervisor Stefano Bonetti for accepting me as master student and for let me enter at Elettra. He gave me the possibility to join his group and let me work in a big facility as a synchrotron. I learnt a lot from his advice both professionally and personally.

The second person I have to thank is my cosupervisor Tevfik Onur Menteş for helping me every day, for trying to teach me as much as i can understand. He supported me from the beginning till the end of the thesis, with strong enthusiasm. Even from Elettra I want to thank Francesca, Andrea and the new joined Mohammad. They are the other members of the Nanospectroscopy. Francesca and Andrea always gave me good advice, I should say that they were my other two cosupervisors.

Now I will list all the people that I think I have to thank, I would love if they prefer to contact me to know why I have to thank them. Random order (women first): Lucile, Martina, Kasturie, Nanna, Francesca again, Vivek, Björn, Neeraj, Matteo, Andrea again and Mohammad, another Matteo from Elettra. All of them, more or less and in a different manner took part in the realization of this work. Last I have to thank a precious friend that helped me to overcome bad days and gave me the streght needed.

Thank you all.

Appendix A

Appendix

Table A.1: Summary of the specifications of the a) beamline and b) SPELEEM located at Nanospectroscopy Elettra Sincrotrone Trieste.

Beamline specifications	
Photon source	2 Apple II type undulators with 20 period of 10 cm
Source size	560 µm x 55 µm (Hor.x Vert.) FWMH
Energy range	10-1000 eV
Polarization	elliptical, linear horizontal and vertical
Beamspot on the sample	30 µm x 10 µm (Hor.x Vert.) @ 16° incident

SPELEEM specifications	
Model	SPELEEM III, Elmitec GmbH
Objective lens	Magnetic triode
Beam separator	symmetrical 120°
Energy filter	Hemispherical, pass energy: 908 eV
Field Limiting Aperture (F.L.A.)	2, 20 µm
Illumination Aperture	0.5, 1, 6 µm (size on sample)
Contrast Aperture	20, 30, 100 µm
Imaging Techniques	LEEM, EELS-LEEM, XANES PEEM, XMC(L)D-PEEM
Diffraction Techniques	μ-LEED, μ-ARUPS, μ-ARPES, μ-EELS, μ-XPD.
Field of Views	LEEM 2-40 µm, XPEEM 2-10 µm
Resolutions	
Real space imaging	10 nm LEEM, 30 nm X-PEEM
Spectral imaging	300 meV
Diffraction imaging	250 meV, lateral resolution defined by F.L.A.
Microprobe spectroscopy	150 meV, lateral resolution defined by F.L.A.

Bibliography

[1] F Genuzio, T O Menteş, and A Locatelli. Magnetization Reversal and Domain Nucleation in Ultra-Thin Co/Re(0001) Capped by Graphitic C. *IEEE Transactions on Magnetics*, 55(2):1–4, 2019.

[2] M P Seah and W A Dench. Quantitative electron spectroscopy of surfaces: A standard data base for electron inelastic mean free paths in solids. *Surface and Interface Analysis*, 1(1):2–11, 1979.

[3] Ernst Bauer. LEEM, SPLEEM and SPELEEM BT - Springer Handbook of Microscopy. pages 487–535. Springer International Publishing, 2019.

[4] MS Altman. Trends in low energy electron microscopy. *Journal of physics: Condensed matter*, 22(8):084017, 2010.

[5] Ernst Bauer. *Surface microscopy with low energy electrons*. Springer-Verlag New York, 1 edition, 2014.

[6] R Diehl, J Ledieu, Nicola Ferralis, A W Szmodis, and Ronan Mcgrath. Low-energy electron diffraction from quasicrystal surfaces. *Journal of Physics: Condensed Matter*, 15(3):R63, jan 2003.

[7] W Telieps and E Bauer. Low energy electron microscopy (leem). In Johannes Friso van der Veen and Michel A Van Hove, editors, *The Structure of Surfaces II*, pages 53–57, Berlin, Heidelberg, 1988. Springer Berlin Heidelberg.

[8] D John O'Connor, Brett A Sexton, and Roger St. C Smart. *Surface Analysis Methods in Materials Science*, volume 23 of *Springer {Series} in {Surface} {Sciences}*. Springer Berlin Heidelberg, Berlin, Heidelberg, 2 edition, 2003.

[9] M.A. van Hove and S.Y. Tong. *Surface Crystallography by LEED, Theory, Computation and Structural Results*. Springer-Verlag Berlin Heidelberg, 1 edition, 1979.

[10] Joachim Stöhr and Hans Christoph Siegmann. *Magnetism*. Springer Berlin Heidelberg, Berlin, Heidelberg, 2006.

[11] Z Q Qiu and S D Bader. Surface magneto-optic Kerr effect (SMOKE). *Journal of Magnetism and Magnetic Materials*, 200(1):664–678, 1999.

[12] Z Q Qiu and S D Bader. Surface magneto-optic Kerr effect. *Review of Scientific Instruments*, 71(3):1243–1255, 2000.

[13] Umesh Tiwari, R Ghosh, and P Sen. Theory of magneto-optic Kerr effects. *Physical Review B*, 49(3):2159, 1994.

[14] S D Bader, E R Moog, and P Grünberg. Magnetic hysteresis of epitaxially-deposited iron in the monolayer range: A Kerr effect experiment in surface magnetism. *Journal of Magnetism and Magnetic Materials*, 53(4):L295–L298, 1986.

[15] F Huang, M T Kief, G J Mankey, and R F Willis. Magnetism in the few-monolayers limit: A surface magneto-optic Kerr-effect study of the magnetic behavior of ultrathin films of Co, Ni, and Co-Ni alloys on Cu(100) and Cu(111). *Physical Review B*, 49(6):3962–3971, feb 1994.

[16] S A Oliver, C A DiMarzio, S C Lindberg, S W McKnight, and A B Kale. Measurement of magnetic fields using the magneto-optic Kerr effect. *Applied Physics Letters*, 63(3):415–417, jul 1993.

[17] Stephan Hüfner. *Photoelectron Spectroscopy*, volume 82 of *Advanced {Texts} in {Physics}*. Springer-Verlag Berlin Heidelberg, third edition, 2003.

[18] Challa S S R Kumar. *Surface Science Tools for Nanomaterials Characterization*. Springer, 1 edition, 2015.

[19] S Doniach and M Sunjic. Many-electron singularity in X-ray photoemission and X-ray line spectra from metals. *J. Phys. C: Solid State Phys.*, 3(2):285–291, feb 1970.

[20] Doon Gibbs, D R Harshman, E D Isaacs, D B McWhan, D Mills, and Ch Vettier. Polarization and resonance properties of magnetic x-ray scattering in holmium. *Physical review letters*, 61(10):1241, 1988.

[21] J P Hannon, G T Trammell, M Blume, and Doon Gibbs. X-ray resonance exchange scattering. *Physical review letters*, 61(10):1245, 1988.

[22] C T Chen, Y U Idzerda, H.-J. Lin, N V Smith, G Meigs, E Chaban, G H Ho, E Pellegrin, and F Sette. Experimental Confirmation of the X-Ray Magnetic Circular Dichroism Sum Rules for Iron and Cobalt. *Physical Review Letters*, 75(1):152–155, 1995.

[23] A Locatelli and E Bauer. Recent advances in chemical and magnetic imaging of surfaces and interfaces by {XPEEM}. *J. Phys.: Condens. Matter*, 20(9):93002, mar 2008.

[24] Eric Beaurepaire, Hervé Bulou, Fabrice Scheurer, and Jean Paul Kappler. *Magnetism: A synchrotron radiation approach*, volume 697. Springer, 2006.

[25] Th Schmidt, S Heun, J Slezak, J Diaz, K C Prince, G Lilienkamp, and E Bauer. SPELEEM: Combining LEEM and spectroscopic imaging. *Surface Review and Letters*, 5(06):1287–1296, 1998.

[26] T O Menteş, G Zamborlini, A Sala, and A Locatelli. Cathode lens spectromicroscopy: methodology and applications. *Beilstein Journal of Nanotechnology*, 5:1873–1886, 2014.

[27] P Vavassori. Polarization modulation technique for magneto-optical quantitative vector magnetometry. *Applied Physics Letters*, 77(11):1605–1607, 2000.

[28] Ioan-Augustin Chioar, Richard Rowan-Robinson, Emil Melander, Tobias Dannegger, Sebastian George, Björgvin Hjörvarsson, Evangelos Th Papaioannou, and Vassilios Kapaklis. Modular magneto-optical diffractometer for the characterization of magnetoplasmonic crystals. 2018.

[29] Theodore C. Oakberg. photoelastic modulators magneto-optic kerr effect. https://www.hindsinstruments.com/wp-content/uploads/Magneto-Optic-Kerr-Effect-Application-Note.pdf.

[30] Matteo Jugovac, Francesca Genuzio, Eduardo Gonzalez Lazo, Nataša Stojić, Giovanni Zamborlini, Vitaliy Feyer, Tevfik Onur Menteş, Andrea Locatelli, and Claus Michael Schneider. Role of carbon dissolution and recondensation in graphene epitaxial alignment on cobalt. *Carbon*, 152(November 2019):489–496, 2019.

[31] Factors influencing graphene growth on metal surfaces. *New Journal of Physics*, 11(6):63046, 2009.

[32] Jan Plutnar, Martin Pumera, and Zdeněk Sofer. The chemistry of CVD graphene. *Journal of Materials Chemistry C*, 6(23):6082–6101, 2018.

[33] Patrick Zeller and Sebastian Günther. What are the possible moiré patterns of graphene on hexagonally packed surfaces? Universal solution for hexagonal coincidence lattices, derived by a geometric construction. *New Journal of Physics*, 16(8), 2014.

[34] Dmitry Usachov, Alexander Fedorov, Mikhail M. Otrokov, Alla Chikina, Oleg Vilkov, Anatoly Petukhov, Artem G. Rybkin, Yury M. Koroteev, Evgueni V. Chulkov, Vera K. Adamchuk, Alexander Grüneis, Clemens Laubschat, and Denis V. Vyalikh. Observation of single-spin Dirac Fermions at the graphene/ferromagnet interface. *Nano Letters*, 15(4):2396–2401, 2015.

[35] Jianmin Xiong, Yunjie Ding, Tao Wang, Li Yan, Weimiao Chen, Hejun Zhu, and Yuan Lu. The formation of Co$_2$C species in activated carbon supported cobalt-based catalysts and its impact on Fischer–Tropsch reaction. *Catal Lett*, 102(3-4):265–269, aug 2005.

[36] A C (Ali Can) Kizilkaya, J W (Hans) Niemantsverdriet, and C J (Kees-Jan) Weststrate. Oxygen Adsorption and Water Formation on Co(0001). *J. Phys. Chem. C*, 120(9):4833–4842, mar 2016.

[37] Raffael Rameshan, Vedran Vonk, Dirk Franz, Jakub Drnec, Simon Penner, Andreas Garhofer, Florian Mittendorfer, Andreas Stierle, and Bernhard Klötzer. Role of Precursor Carbides for Graphene Growth on Ni(111). *Scientific reports*, 8(1):2662, 2018.

[38] Dmitry Yu. Usachov, Kirill A Bokai, Dmitry E Marchenko, Alexander V Fedorov, Viktor O Shevelev, Oleg Yu. Vilkov, Elmar Yu. Kataev, Lada V Yashina, Eckart Rühl, Clemens Laubschat, and Denis V Vyalikh. Cobalt-assisted recrystallization and alignment of pure and doped graphene. *Nanoscale*, 10(25):12123–12132, 2018.

[39] E Miniussi, M Pozzo, A Baraldi, E Vesselli, R R Zhan, G Comelli, T O Mente\ifmmode \mbox\cs\else \cs\fi, M A Niño, A Locatelli, S Lizzit, and D Alfè. Thermal Stability of Corrugated Epitaxial Graphene Grown on Re(0001). *Phys. Rev. Lett.*, 106(21):216101, 2011.

[40] E Miniussi, M Pozzo, T O Menteş, M A Niño, A Locatelli, E Vesselli, G Comelli, S Lizzit, D Alfè, and A Baraldi. The competition for graphene formation on Re(0001): A complex interplay between carbon segregation, dissolution and carburisation. *Carbon*, 73:389–402, 2014.

[41] S. Vlaic, A. Kimouche, J. Coraux, B. Santos, A. Locatelli, and N. Rougemaille. Cobalt intercalation at the graphene/iridium(111) interface: Influence of rotational domains, wrinkles, and atomic steps. *Applied Physics Letters*, 104(10), 2014.

[42] Francesca Genuzio, Pietro Genoni, Tevfik Onur Menteş, Benito Santos, Alessandro Sala, Cristina Lenardi, and Andrea Locatelli. Stimulated CO Dissociation and Surface Graphitization by Microfocused X-ray and Electron Beams. *Journal of Physical Chemistry C*, 2019.

[43] N. Rougemaille, A. T. Ndiaye, J. Coraux, C. Vo-Van, O. Fruchart, and A. K. Schmid. Perpendicular magnetic anisotropy of cobalt films intercalated under graphene. *Applied Physics Letters*, 2012.

[44] K De'Bell, A B MacIsaac, and J P Whitehead. Dipolar effects in magnetic thin films and quasi-two-dimensional systems. *Reviews of Modern Physics*, 72(1):225–257, jan 2000.

[45] T Thomson. Magnetic properties of metallic thin films. In *Metallic Films for Electronic, Optical and Magnetic Applications*, pages 454–546. Elsevier, 2014.

[46] Robert C O'handley. *Modern magnetic materials: principles and applications*. Wiley, 2000.

[47] J Stöhr. Exploring the microscopic origin of magnetic anisotropies with X-ray magnetic circular dichroism (XMCD) spectroscopy. *Journal of Magnetism and Magnetic Materials*, 200(1-3):470–497, 1999.

[48] Hongxin Yang, Anh Duc Vu, Ali Hallal, Nicolas Rougemaille, Johann Coraux, Gong Chen, Andreas K Schmid, and Mairbek Chshiev. Anatomy and Giant Enhancement of the Perpendicular Magnetic Anisotropy of Cobalt–Graphene Heterostructures. *Nano Letters*, 16(1):145–151, jan 2016.

[49] C M Schneider, P Bressler, P Schuster, J Kirschner, J J de Miguel, and R Miranda. Curie temperature of ultrathin films of fcc-cobalt epitaxially grown on atomically flat Cu(100) surfaces. *Physical Review Letters*, 64(9):1059–1062, feb 1990.